

# A Simplified Gravitational Reference Sensor for Satellite Geodesy

Anthony Dávila Álvarez<sup>1</sup> · Aaron Knudtson<sup>1</sup> · Unmil Patel<sup>1</sup> · Joseph Gleason<sup>1</sup> · Harold Hollis<sup>1</sup> · Jose Sanjuan<sup>1</sup> · Neil Doughty<sup>2</sup> · Glenn McDaniel<sup>2</sup> · Jennifer Lee<sup>2</sup> · James Leitch<sup>2</sup> · Stephen Bennett<sup>2</sup> · Riccardo Bevilacqua<sup>3</sup> · Guido Mueller<sup>1</sup> · Robert Spero<sup>4</sup> · Brent Ware<sup>3</sup> · Peter Wass<sup>1</sup> · David Wiese<sup>4</sup> · John Ziemer<sup>4</sup> · John W. Conklin<sup>1</sup>

18 July 2021

**Abstract** The University of Florida, in collaboration with Caltech/JPL, Ball Aerospace, and Embry-Riddle Aeronautical University has developed a Simplified Gravitational Reference Sensor (S-GRS), an ultra-precise inertial sensor for future Earth geodesy missions. These sensors are used to measure or compensate for all non-gravitational accelerations of the host spacecraft so that they can be removed in the data analysis to recover spacecraft motion due to Earth's gravity field, which is the main science observable. Low-low satellite-to-satellite tracking missions like GRACE-FO that utilize laser ranging interferometers are technologically limited by the acceleration noise performance of their electrostatic accelerometers and temporal aliasing associated with Earth's dynamic gravity field. The current accelerometers, used in the GRACE and GRACE-FO missions have a limited sensitivity of  $\sim 10^{-10} \text{ m/s}^2/\text{Hz}^{1/2}$  around 1 mHz. The S-GRS is estimated to be at least 40 times more sensitive than the GRACE accelerometers and over 500 times more sensitive if operated on a drag-compensated platform. The improved performance is enabled by increasing the mass of the sensor's test mass, increasing the gap between the test mass and its electrode housing, removing the small grounding wire used in the GRACE accelerometers and replacing them with a UV

LED-based charge management system. This level of improvement allows future missions to fully take advantage of the sensitivity of the GRACE-FO Laser Ranging Interferometer (LRI) in the gravity recovery analysis. The S-GRS concept is a simplified version of the flight-proven LISA Pathfinder (LPF) GRS. Performance estimates are based on models vetted during the LPF flight and the expected Earth orbiting spacecraft environment based on flight data from GRACE-FO. The relatively low volume ( $\sim 10^4 \text{ cm}^3$ ), mass ( $\sim 13 \text{ kg}$ ), and power consumption ( $\sim 20 \text{ W}$ ) enables the use of the S-GRS on ESPA-class microsatellites, reducing launch costs or enabling larger numbers of satellite pairs to improve the temporal resolution of Earth gravity field maps. The S-GRS design and analysis, as well as its gravity recovery performance when implemented in two candidate mission architectures, are discussed in this article.

**Keywords** Satellite Geodesy · Gravity Measurements · Accelerometers

## 1 Introduction

Precision inertial sensing is important for many space science missions, including fundamental physics experiments (Everitt et al 2011; Touboul et al 2001) and gravitational wave observation (Danzmann and Rüdiger 2003). The S-GRS presented here specifically targets future satellite geodesy missions, following the successful CHAMP (Reigber et al 2002), GRACE (Tapley et al 2004), GOCE (Drinkwater et al 2003), and GRACE-FO (Sheard et al 2012) missions.

The GRACE (2002-2017) and GRACE-FO (2018-present) missions in particular have provided a nearly 20-year climate data record of Earth system mass-changes.

John W. Conklin

<sup>1</sup>University of Florida, Gainesville, FL 32611

E-mail: jwconklin@ufl.edu

<sup>2</sup>Ball Aerospace, Broomfield, CO 80021

<sup>3</sup>Embry-Riddle Aeronautical University, Daytona Beach, FL 32114

<sup>4</sup>Caltech/Jet Propulsion Laboratory, Pasadena, CA 91109

The utility of the data is incredibly diverse for addressing both scientific hypothesis and serving societal applications. Contributions include quantifying the rate of ice sheet and glacier ablation globally, identifying and quantifying areas of unsustainable groundwater withdrawal due primarily to heavy irrigation, quantifying global and regional sea level changes and ocean heat content (when combined with satellite altimetry), monitoring drought severity through operational assimilation in the U.S. Drought Monitor, and assessment of geohazards, including mapping mass redistributions due to large earthquakes (Tapley et al 2019). The importance of mass change observations was recognized in the 2018 Decadal Survey for Earth Science and Applications from Space, where Mass Change was listed as a Designated Observable (National Academies of Sciences Engineering and Medicine 2018), and is now a core component of NASA’s Earth System Observatory to be launched in the next decade.

The quality of mass change data products derived from a gravity mission depends on the orbital characteristics of the mission (altitude, inclination, number of satellite pairs, etc.), as well as the precision of the on-board measurement system (inter-satellite ranging system, accelerometer, attitude and orbit determination). For GRACE-FO, it is well understood that the limiting source of error is due to temporal aliasing; i.e. under-sampling of high frequency mass variations in the Earth system such as ocean tides and weather systems (Fig. 1, top). There are two possible ways to reduce the impact of temporal aliasing error on derived gravity fields: 1) sample more frequently via more satellite pairs (Daras and Pail 2017; Elsaka et al 2013; Wiese et al 2011b,a,c) as shown in Fig. 1 (bottom), and 2) process the data in an ‘along-the-orbital track’ approach rather than accumulating observations over a finite number of days, which is traditionally done. Solution 1) is well understood, having been extensively studied in the literature, while solution 2) is less well understood but recent analysis suggests it is a promising approach. For example, first ‘along-the-orbital track’ analysis of the GRACE-FO LRI data revealed exquisite detail in static gravity field features otherwise not seen in traditional data analysis approaches (Ghobadi-Far et al 2020; Han et al 2021a,b).

Future mission implementations should seek to minimize the impact of temporal aliasing error via one of the above two solutions. The precision of the accelerometer becomes important in such a design, as those in GRACE-FO limit both approaches. The precision of the GRACE-FO electrostatic accelerometers is insufficient for a multi-pair implementation (Fig. 1 bottom. green dashed curve) at lower altitudes ( $\sim 350$  km), and

dominates over all other error terms. The S-GRS offers a technological pathway to improve the measurement of non-gravitational accelerations (Fig. 1, bottom) to an acceptable level for such constellation-type implementation. Furthermore, and perhaps even more importantly, the S-GRS offers a technological solution to measuring non-gravitational forces at a level that is on par with the precision of the LRI that was successfully demonstrated on GRACE-FO (Fig. 1 shows comparable magnitude for the blue and red-dashed curves) (Abich et al 2019). Such a match in performance between the accelerometer and the inter-satellite ranging instrument has potential to allow for full exploitation of the data in future ‘along-the-orbital track’ data analysis, as discussed in (Spero 2021). The current mismatch in performance between the LRI and the accelerometer on GRACE-FO limits interpretation of ‘along-the-orbital track’ signals to smaller spatial scales only; such analysis is currently not valid for the longest wavelengths in the gravity field, where the accelerometer error is dominant (Ghobadi-Far et al 2018), and the signal amplitudes are the largest.

Figure 2 uses methods described in (Hauk and Wiese 2020) to show the maximum potential improvement the S-GRS offers in the architectures listed in Fig. 1. Maximum scientific potential can be assessed by looking at the measurement system performance (neglecting temporal aliasing error); this assumes temporal aliasing error is mitigated via ‘along-the-orbital track’ data analysis or future improvements in models of high frequency mass variations. The potential for improvement offered by the S-GRS in the dual-pair architecture, in particular, could advance the measurement parameters beyond those targeted in the Decadal Survey and identified in the Baseline Measurement Parameters in the Science and Applications Traceability Matrix identified by the Mass Change (MC) Study Team for the next observing system implementation (NASA 2020a,b).

### 1.1 Simplified Gravitational Reference Sensor

The S-GRS design follows that of the flight-proven LPF Gravitational Reference Sensor (GRS) that represents the state of the art in precision inertial sensors (Dolesi et al 2003). The LPF GRS uses a 2 kg, Au/Pt test mass (TM) inside a molybdenum electrode housing (EH). The housing holds 12 gold-coated electrodes to differentially sense the position and orientation of the cube via capacitive sensing and to control it using electrostatic actuation. Six “injection electrodes” are driven with a 100 kHz AC bias voltage to frequency shift the capacitive measurement to high frequency. The 4 mm gap (in LPF) between the TM and housing is defined by a

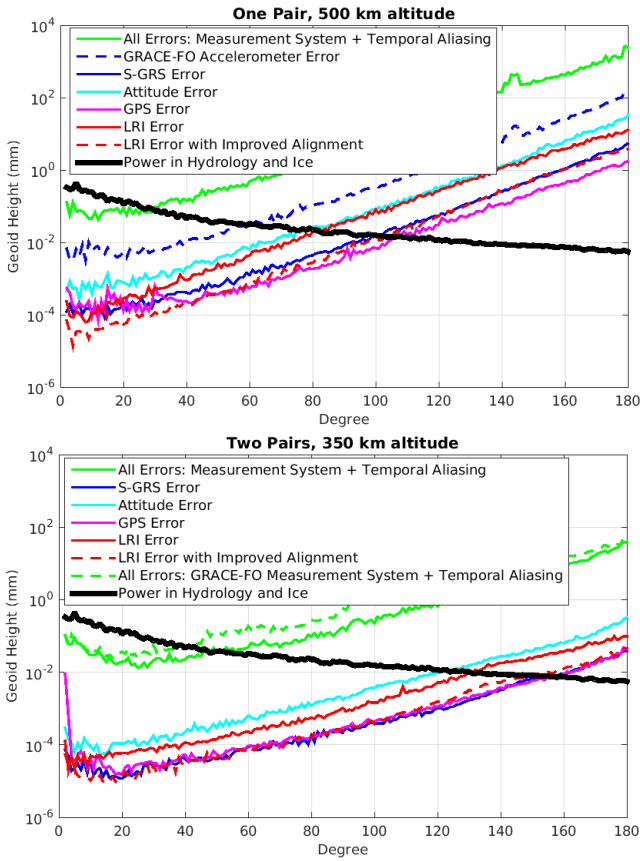


**Fig. 1** Figure 1. Monthly gravity field error budget (1a) for a single pair of satellites at 500 km altitude in a polar orbit with no drag compensation and (2a) an architecture consisting of two pairs (one polar, one inclined at 70 deg) at 350 km altitude with full drag compensation in the flight direction. The error (units: mm of geoid height) of each instrument and its impact on the recovered gravity field per spherical harmonic degree is shown, as derived from numerical simulations. Simulation details are provided in Appendix A

trade-off; it is large enough to reduce noise sources, such as uncontrolled potentials on the electrodes, and small enough to measure TM displacement at the nanometer-level over the measurement bandwidth. A caging and venting mechanism uses a series of mechanical fingers to secure the TM during launch and release it in orbit (Bortoluzzi et al 2013). During science operations, the TM charge is controlled by a charge management system (CMS) based on UV photoemission using Hg vapor lamps as the UV source (Armano et al 2018a). The CMS eliminates the need for the small grounding wire used in the ONERA accelerometers that both limits their performance and causes challenges during integration and testing (Touboul et al 1999).

The primary performance metric for these instruments is the acceleration noise from the residual spurious forces acting on the TM, often defined by an amplitude spectral density (ASD). LPF, launched in 2015,

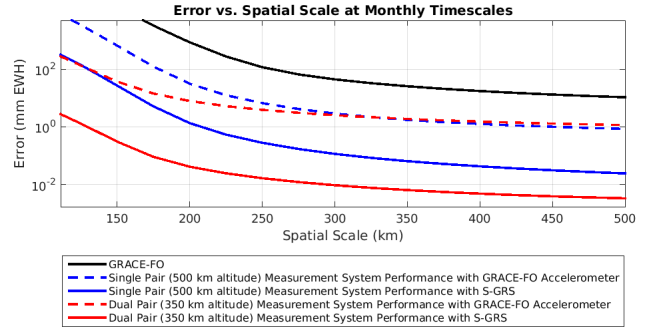


**Fig. 2** Error in mm equivalent water height (EWH) versus spatial scale for monthly time resolutions, comparing measurement system performance with the S-GRS versus pre-flight error estimates from the GRACE-FO accelerometers as derived from numerical simulations. Note the blue and red curves neglect temporal aliasing error, showing the maximum potential improvement, while the black curve includes temporal aliasing error as well as instrument error models for the LRI, accelerometer, GPS, and attitude determination system, and as such is indicative of the performance of the GRACE-FO monthly gravity fields.

exceeded requirements by more than a factor of ten with a measured acceleration noise below  $3 \times 10^{-15} \text{ m/s}^2/\text{Hz}^{1/2}$  between 0.4 mHz and 20 mHz (Armano et al 2018b), the same frequency band that is important for Earth geodesy. This represents a factor of  $3 \times 10^4$  improvement over the performance of GRACE and GRACE-FO and  $10^3$  over that of the GOCE instrument (Christophe et al 2010).

The S-GRS is a scaled-down version of the LPF GRS, with reduced mass and complexity, and it is optimized with respect to performance for future geodesy missions (see Fig. 1). Key features of the design and its implementation that improve sensitivity with minimal size, mass, and power are:

- The TM grounding wire used in previous accelerometers is removed, TM charge is instead controlled via non-contact UV photoemission as in LPF. The grounding wire is one primary source of acceleration noise in current electrostatic accelerometers.
- Removing this grounding wire allows us to increase the TM-to-EH gap from  $\sim 100 \mu\text{m}$  to  $\sim 1 \text{ mm}$ , as well as the TM mass from  $\sim 100 \text{ g}$  to  $> 500 \text{ g}$ . Acceleration noise performance scales linearly with TM mass and, to first order, with the gap size between the TM and EH.
- Careful control of the environment surrounding the TM, including venting to space to reduce residual pressure, and shielding against Earth's magnetic field and thermal fluctuations.

- Tightly integrating the S-GRS and LRI, eliminating the microwave ranging instrument used on GRACE-FO to minimize size, mass, and power.
- Design for the possibility of operating the S-GRS on a drag-compensated platform to further reduce acceleration noise, while simultaneously maintaining orbit altitude.

The instrument consists of an S-GRS Head and an Electronics Unit. The detailed CAD design of the S-GRS Head is shown in Fig. 3. It is the mechanical unit containing the TM and EH, the caging mechanism, and the vacuum enclosure with a retroreflector or triple mirror assembly similar to the one on GRACE-FO. The Electronics Unit performs all control and read-out functionalities and is separated from the S-GRS head to minimize electromagnetic and thermal disturbances to the TM. In the remaining sections of the paper each sub-element of the S-GRS will be described beginning with the S-GRS head in Section 2 and the S-GRS electronics unit in Section 3. In Section 4 we present a breakdown of the S-GRS acceleration noise performance followed by simulations of the test-mass position control algorithms in Section 5 and conclusions in Section 6.

## 2 S-GRS Head

### 2.1 Test mass and electrode housing

Detailed performance analyses determined that a 30 mm cubic Au-Pt TM with a mass of 540 g results in the desired acceleration noise performance described in Section 4, while keeping mass and volume of the sensor to a minimum. The TM is a perfect cube, coated in gold, except for two indented features on opposite sides, one conical and the other pyramidal, where the caging mechanism constrains it.

The electrode housing design is a scaled-down version of the LISA-like EH prototype previously fabricated by the UF team and shown in Fig. 4. The inner dimension of the cubic EH is 32 mm creating a 1 mm gap between the TM and EH, and its wall thickness is approximately 10 mm. The technology readiness level (TRL) 5 EH will be fabricated from gold-coated molybdenum with sapphire electrode spacers. Molybdenum is chosen for its low magnetic properties, machinability, and high thermal conductivity, which reduces thermal gradients across the sensor. Sapphire is chosen because its coefficient of thermal expansion is nearly the same as that of molybdenum.

The electrode geometry, shown in Fig. 5, differs from that of LPF. The S-GRS design has one large electrode

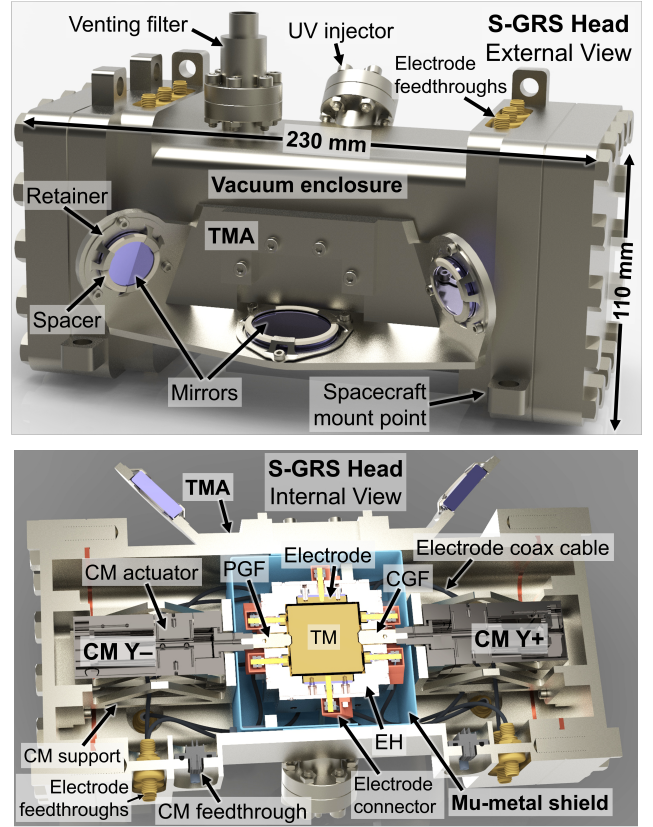


**Fig. 3** S-GRS Head CAD rendering external view (top) and internal view (bottom). CM: Caging Mechanism, PGF: Pyramidal Grabbing Finger, CGF: Conical Grabbing Finger, TM: Test Mass, EH: Electrode Housing, TMA: Triple Mirror Assembly.

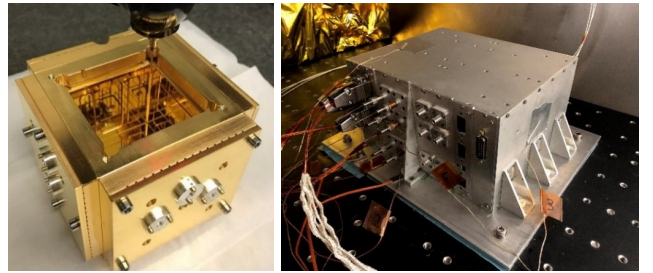


**Fig. 4** LISA-like EH prototype (left) and TRL 5 LISA CMS during thermal-vacuum (TVAC) testing at UF (right). The S-GRS EH and Electronics Unit are based on these designs.

along the sensitive axis aligned with the LRI, which maximizes sensitivity in this direction and minimizes cross coupling with other degrees of freedom. Around the holes used for the CM fingers, both faces normal to the Y-axis have 2 injection signal electrodes and 2 sensing electrodes that can measure TM rotation along the Z-axis. Faces normal to the Z-axis have 1 injection electrode and 4 sensing electrodes to detect TM rotation along the X and Y axes.



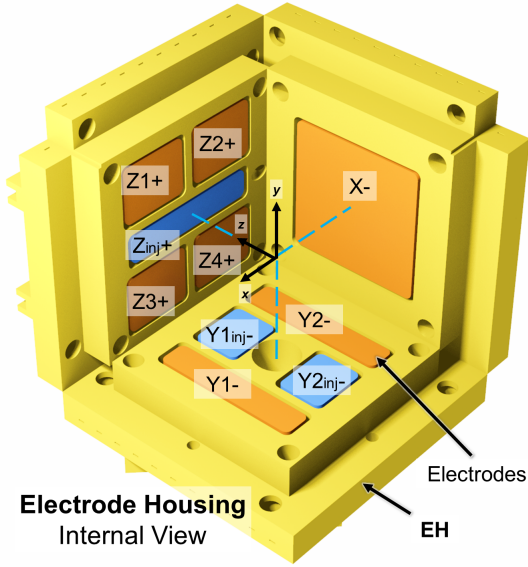


**Fig. 5** Internal view of the EH with labeled electrodes. Blue electrodes are connected to the injection signal, while orange ones are used for sensing and actuation.

## 2.2 Triple Mirror Assembly

The Triple Mirror Assembly (TMA), shown in Fig. 6, is an optics mounting structure located on the +X face of the vacuum enclosure (see Section 2.3). It acts as a retroreflector at the ends of the “racetrack” configuration for the LRI that measures the distance between the pair of satellites (Dahl et al 2017). The input beam is reflected in three orthogonal planes, producing an output beam at an offset distance in an anti-parallel orientation. The TMA is designed so that the virtual vertex at which the three planes intersect is coincident with the center of mass of the spacecraft’s inertial reference body, the TM, when it is located in the center of the EH. This way, the LRI’s distance measurement is done between the reference masses of each satellite.

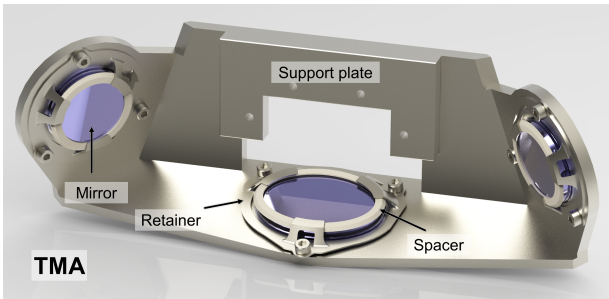


**Fig. 6** Close-up of the TMA and its components.

The concept for the TMA is based on an equivalent component of the GRACE-FO mission (Abich et al

2015; Kornfeld et al 2019). The corner-cube principle is similarly implemented in both designs, with the purpose of returning the LRI beam, regardless of pointing variations. A difference in the design concept comes from the fact that in GRACE-FO the TMA was used as a technology demonstrator and was not the ranging instrument. A Ka-band microwave interferometric system and cold-gas tanks were located in the line-of-sight section of the S/C, making the offset between the LRI input and output beams a design driver for the TMA. This resulted in a long tube-like structure that supported the three mirroring surfaces. Since this is assumed to not be the case for the S-GRS, the beam offset distance is smaller and defined by the size of the EH, resulting in a more compact TMA geometry.

The TMA is made of titanium alloy, with three sapphire mirrors supported by titanium alloy retainers and PEEK spacers. Since the TMA is essentially a corner-cube, the geometry is based on the three intersecting sides of a cube with its vertex located at the TM center. This cube has a yaw angle of  $45^\circ$  from the chamber wall for a symmetric aperture of the mirrors in the input and output planes. It also has a pitch angle of  $20^\circ$  that reduces the volume of the body that supports the mirrors. There is a mean distance of 129 mm between the input and output beams.

An advantage of the symmetric geometry of the TMA and its large contact area with a chamber wall of the same material, is the athermal behavior on the vertex position with respect to the TM center. Any thermal deformation of the chamber would similarly affect the TMA planes, reducing any changes in the vertex position. The goal is to maintain the TMA vertex within  $50 \mu\text{m}$  of the TM center and a co-alignment error of less than  $50 \mu\text{rad}$ .

## 2.3 Vacuum Enclosure

The S-GRS electrode housing and TM are enclosed within a vacuum enclosure, shown in Figure 3 to limit the effects of Brownian noise and improve the sensing system’s noise environment (McNamara et al 2013) with a goal pressure of  $10^{-5}$  Pa. While on ground, the enclosure can be pumped out for testing purposes. On orbit, residual gas in the chamber will be vented to space through a duct to separate the system from the outgassing of the rest of the vehicle. The chamber is also the main supporting structure; the TM is located at its center, the upper and lower sections of the caging mechanism are positioned on opposite sides of the EH, and the TMA is mounted on the external +X face of the enclosure (see Section 2.2).

The vacuum enclosure is designed to support the TMA on its exterior and contain the TM, EH, caging mechanism, magnetic shield, and their supports. The EH is fastened and aligned through its frame to stiffener-like surfaces within the chamber that are placed away from the TM center. These surfaces are also used to support the standoffs and fasteners for the magnetic shield that surrounds the EH. Twenty coaxial SMA feedthroughs that connect to the EH electrodes are distributed around the top and bottom sections of the enclosure, except on the TMA face. Two D-Sub 25 pin feedthroughs that connect to the caging mechanism actuators are placed on the -X face. The UV injector is attached to a CF flange located at the central section of the enclosure between the +Z and -X faces at a 45 deg angle along the +Y axis. The enclosure enclosure vent duct is attached to a flange on the +Z face.

The chamber is based on the LPF design but with a smaller size and rectangular shape. The 5 mm thick walls were selected to keep the maximum deformation from pressure and thermal loads below 10  $\mu\text{m}$ . With the ConFlat-type (CF) square ends, the chamber is 235 mm long with an internal square section of 78 mm at the center.

The UV injector feedthrough and flange are based on commercially available CF options, similar to the one used in the LISA Inertial Sensor UV Kit (ISUK) (Armano et al 2018a). The 65 mm injector is supported at the flange and extends through a hole on the EH. The diameter and length of the injector is such that no additional support is required to avoid any collisions to the EH during launch. The central location along the Y axis is required so that the UV light is reflected at a 45 deg angle of incidence between the TM and the +Z injection electrode of the EH.

In addition to the protective walls of the vacuum enclosure, a magnetic shield is required to attenuate the magnetic field at the TM (see Fig. 3). The cubic shield fully envelops the sensor with the exception of gaps for the support stiffeners and holes for the caging mechanism grabbing fingers (GF), coaxial cables, UV injector, and shield fasteners. Acceleration noise modeling described in Section 4 shows that attenuation of the Earth's magnetic field by at least a factor of ten is needed to meet performance goals.

## 2.4 Caging Mechanism

The caging mechanism must secure the TM against launch loads and gently release it once in orbit. The technical challenge is that upon release, the TM must have a low enough velocity relative to the spacecraft so that the S-GRS control system can electrostatically

capture it. To achieve such a low relative velocity, the design must minimize both adhesion between the GF and TM gold surfaces, and any asymmetry in the mechanical preloads just prior to release (Bortoluzzi et al 2013). The S-GRS caging mechanism, designed by Ball Aerospace and simulated by the UF team, reduces the three-stage LISA system to a simpler two-stage system. The first stage uses standard aerospace launch lock actuators to handle launch loads, while the second stage utilizes a commercial vacuum-compatible piezo-walker motor. The first stage applies 200 N to a pair of opposing titanium alloy, hard gold plated fingers that engage the TM at the conical and pyramidal indents, as seen in Fig. 7.

After the one-time first stage launch lock is released, the second stage retracts the gold alloy fingers until the TM is held with a  $<1\text{ N}$  preload by spring-loaded release tips (RT), as seen in Fig. 8. The spring stiffness is designed to ensure that the adhesion between the gold-coated TM and the gold alloy fingers is broken. The final RTs are fabricated from a hard, non-stick silicon nitride material to avoid adhesion with the TM. Damping is added to the system so that the TM motion is minimized upon final retraction and release. To minimize potential electrostatic interactions between the silicon nitride RTs and the TM, the caging mechanism retracts the tips  $\sim 10\text{ mm}$  inside the EH.

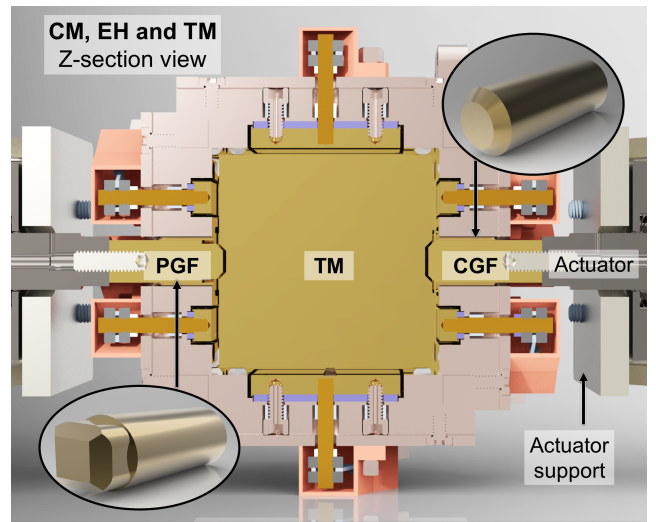


**Fig. 7** Section view of the CM around the EH and TM. The shapes of the PGF and CGF tips are shown.

The simplification to a two-stage system is possible because of the lighter 0.54 kg mass of the S-GRS TM compared to the 1.96 kg LPF TM. Static and random vibration FEA simulations validate the use of only two fingers to support the TM during launch. The static simulations apply a 15  $g$  acceleration to the system in

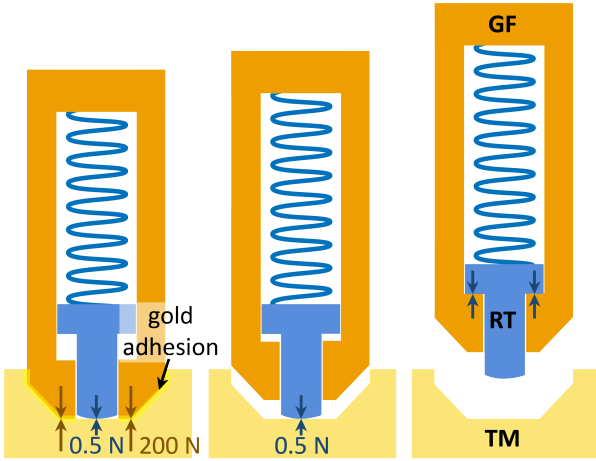


**Fig. 8** Spring-tip concept release process. First, the GF applies a 200 N to the TM, As the GF retracts (center), a 0.5 N preload applied by the RT breaks the gold adhesion. Finally, the RTs damp the TM motion until they are fully retracted.

three orthogonal directions. The random vibration simulations use the  $14.1 g_{rms}$  ASD from the NASA GEVS document (NASA 2021). The result proves the feasibility of the two-finger approach with a high margin of safety. The 200 N holding force safely satisfies the low TM displacement requirements, especially for the critical case of random vibration along the Y-axis (along the length of the fingers).

In addition to its caging capabilities, the mechanism must also release the TM at a low residual velocity. A maximum allowable residual velocity is obtained from a 2 DOF dynamics simulation that starts immediately after the TM is released and stops when it has been captured by the electrostatic actuation system or collides with the EH. The simulation iterates through a range of initial TM linear and angular velocities, actuation voltages, and directions of motion. The objective is to find the highest initial velocity values that can still be captured by the actuator system. In the model, the TM is treated as a square of four rigidly grouped particles that represent its four corners in the plane of motion. As the square moves because of its initial velocity, the actuator system applies a force that attempts to cancel the TM motion. The electrostatic force is a non-linear function, dependent on the voltage and distance between the TM and actuator electrodes, and the electrode area (Ciani 2008). Since the S-GRS has different electrode configurations on each face, the electrode areas and locations vary for each plane of motion. The greater the electrode area and the smaller the gap to the TM, the higher the actuation force. Assuming a 10 V actuation voltage, the residual linear velocity must be  $<4.5 \mu\text{m/s}$  and the angular residual velocity  $<291 \mu\text{rad/s}$ .

With a known residual velocity requirement, a second dynamics model is created to simulate the actual retraction and release process. The 1 DOF model is based on that used for the LPF Grabbing Positioning and Release Mechanism (GPRM) (Bortoluzzi et al 2013) but with the Ball Aerospace spring-tip concept. The system uses the retraction speed of both GFs as an input and simulates the RT and TM dynamics. Assuming all conditions are symmetric between both sections of the caging mechanism, the result is an ideal release where the TM remains centered in the EH. It is only when asymmetries are included in the system, that the TM drifts to one direction. The worst-case scenario for this asymmetry involves having the maximum adhesion force profile on one GF and no adhesion with a retraction delay on the other. The retraction asymmetry causes a kick from the delayed GF, which acts like a compressed spring (Bortoluzzi et al 2016). The one-sided adhesion force keeps the TM attached to only one GF, pulling the TM as it is retracted. This requires assuming that the gold adhesion force profiles described in the GPRM model apply between the GF and TM. Other than the mechanical spring and damping forces between the GFs and their respective RTs, all bodies in contact are treated as compressed springs to simulate contact forces with the penalty method. An additional electrostatic spring-like force acts upon the TM and is a function of the squared sensing injection bias (Ciani 2008).

The model's output contains the location, velocity, and forces of each component along the Y-axis (direction of release). These can be used to identify the necessary spring and damping coefficients, retraction velocity, and understand the performance of the current design. The spring-tip concept worst-case simulation uses the 200 N preload, a  $50 \mu\text{s}$  delay (as used in the GPRM model), and the strongest adhesion force profile on one GF. For the resulting time series on Figure 9, a damping ratio of 3, a spring constant of 131 N/m, an initial actuator speed of  $50 \mu\text{m/s}$ , and an injection signal bias of 4 V is used. In the figure, a time series describes the displacement, speed and the GF to TM contact forces. Initially, the GFs are preloaded against the TM until retraction starts. Because of the adhesion force, the TM sticks to GF2 as it is retracted (seen in point 1 of the top plot). In point 2, RT1 is pulled back by GF1 as it is constrained by its geometry inside the GF. This decreases RT1's preload to the TM, allowing RT2 to push the TM and break the adhesion force. With no contact between the GFs and TM, the retraction speed is decreased at point 3 to extend the time in which the RTs dissipate the TM kinetic energy. As seen in the middle plot, the TM speed amplitude decays while GF retraction con-

tinues. At point 4, both RTs are constrained and pulled by their respective GFs until the TM is fully released in point 5.

The adhesion force profile and retraction delay time would be random and uncontrollable inputs in the actual release process, so a Monte Carlo simulation is used to determine the probability of safe release. The adhesion force maxima ranges from 0.1 to 0.15 N. The elongation or separation between the bonded surfaces in which the maximum force occurs varies from 0.4 to 0.8  $\mu\text{m}$ . The retraction delay time ranges from 0 to 100  $\mu\text{s}$ . Using a damping ratio of 3 and assuming all three random inputs are uniformly distributed, results in a mean TM residual velocity of 1.11  $\mu\text{m/s}$  with a standard deviation of 0.67  $\mu\text{m/s}$  for 100 points. A histogram of the results can be seen in Fig. 10, where the TM is safely released for all points with a minimum safety factor of 1.7 in the right-most bar.

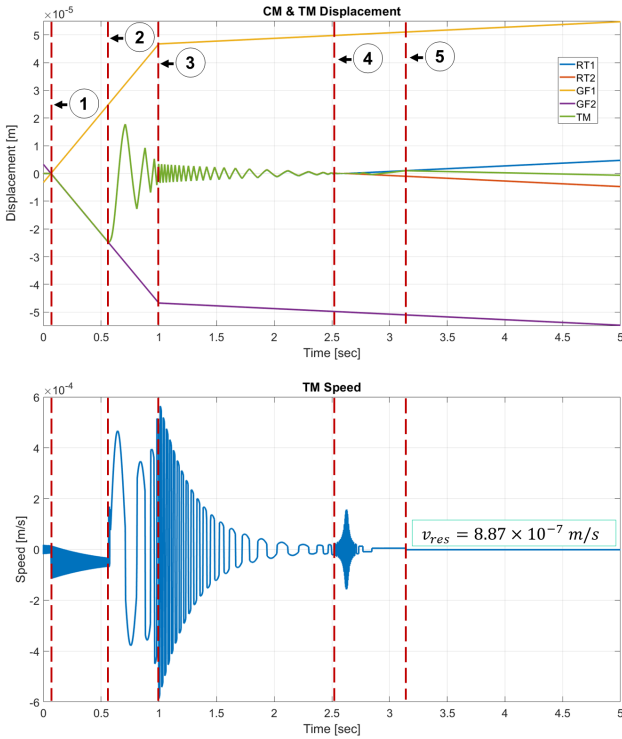


**Fig. 9** Time series of the spring-tip concept release simulation. The top plot shows the displacement of each component along with labels for the described events. The TM speed oscillates as its motion is dissipated by the RTs bottom).

## 2.5 Charge Management System

The University of Florida team has been developing the LISA CMS for over four years (Kenyon et al 2021).



**Fig. 10** Histogram of TM residual speed from a 100 point Monte Carlo analysis.

The CMS utilizes newer UV LEDs that both resolve technical issues related to the Hg-lamp system used by LPF, and reduce the SWaP of this subsystem. Compared to the Hg lamps used in LPF, UV LEDs are smaller, lighter, consume less power, and have a higher dynamic range, with at least an order of magnitude improvement in each performance area (Olatunde et al 2015). The S-GRS will use an advanced pulsed, continuous charge control scheme with a low power (nW) UV light, pulsed in a low duty cycle that is synchronized to the 100 kHz injection electric field (Inchauspé et al 2020). Photoelectron flow between the TM and EH will anti-align with the injected field, causing the phase of the UV light pulses with respect to the field to determine the net flow of photoelectrons and the resulting equilibrium charge of the TM. The UV pulse phase is then selected to produce a passively stable TM equilibrium charge of 0 Coulombs.

The CMS unit, shown in Figure 4, consists of an FPGA-based controller, a power system, the UV LEDs and their current sources, a mechanical enclosure, and a fiber optic harness that delivers the UV light to the S-GRS head. The LISA CMS will reach TRL 5 in September 2021 and TRL 6 by the end of 2022. In terms of S-GRS development, the CMS only needs to be tested in integration with the TM and EH because of the difference in geometry to the LISA GRS. In addition to being smaller in size, the S-GRS will only have a single UV light feedthrough (instead of three for LISA) that will be oriented to maximize discharge robustness against variations of the gold surfaces of the TM and EH.

## 3 Electronics Unit

The S-GRS electronics, which comprises both analog and digital elements, must perform the following functions:



- Generate (digitally) the TM injection bias to frequency shift the capacitive readout from low frequency to the injection frequency (100 kHz)
- Perform the six degree of freedom position readout of the TM by differencing opposing pairs of sensing/actuation electrodes via analog electronics, and demodulating the differenced signals at the injection frequency via digital electronics
- Apply actuation voltages via a digital-to-analog converter to the sensing and actuation electrodes at audio frequencies to control the position and orientation of the TM
- Drive the current source for the UV LEDs to discharge the TM
- Drive the caging and positioning mechanism

The S-GRS can be operated in two primary modes: drag-compensation and accelerometer mode. In accelerometer mode, all control algorithms are embedded within the S-GRS so that it may be treated as a black box that provides spacecraft acceleration estimates. The TM position and orientation is estimated and a control algorithm commands the actuation system to keep the TM centered in its housing. The command forces applied to the TM and the residual spacecraft to TM motion are used to estimate the non-gravitational spacecraft acceleration. In this mode, no spacecraft propulsion is required.

Drag-compensation is a spacecraft-level control loop that commands thrusters using S-GRS data to keep the spacecraft centered on the TM without applying actuation forces to the TM. In this mode, external forces on the spacecraft are directly canceled by a propulsion system, minimizing the applied forces and therefore the force noise on the TM. In addition to improved acceleration noise performance, drag-compensation also simplifies the data analysis, since there is no non-gravitational spacecraft acceleration that must be accounted for. For an infinite-gain closed-loop system, the TM position signal is zero but the noise levels of the measurement will limit the performance of the loop and, consequently, the ability to measure non-inertial forces in accelerometer mode or minimize them in the drag-free configuration.

### 3.1 Capacitive Sensing Electronics

The TM position in the EH is measured by the capacitive sensing electronics. The basic principle consists of measuring the differential changes between the capacitances on opposite sides of the TM. Similarly, the rotation of the TM can be measured by combining the information of electrode pairs.

One of the limiting noise sources is the intrinsic noise in the capacitive sensing electronics. The main goal is to reach noise levels on par with the GRACE-FO LRI system, i.e., around  $1 \text{ nm/Hz}^{1/2}$  in the frequency range of approximately 0.35 mHz to 50 mHz. The proposed capacitive sensor electronics system is shown in Fig. 11. It is based on an AC differential charge amplifier (Lotters et al 1999) unlike the differential transformer designs used in other accelerometers (Josselin et al 1999; Speake and Andrews 1997; Weber et al 2002).

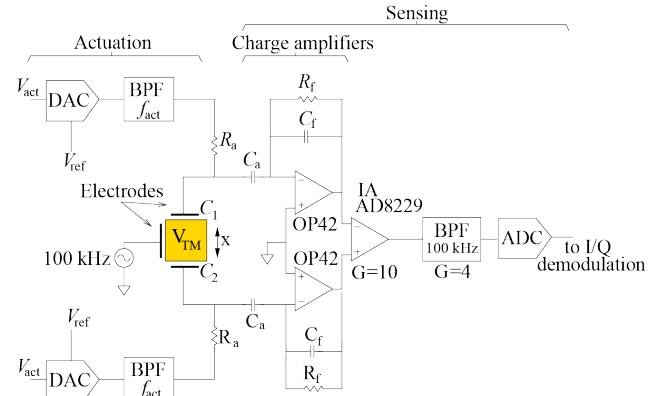


**Fig. 11** Capacitive sensing and actuation electronics for one degree of freedom. Two charge amplifiers (with  $C_f=10 \text{ pF}$  and  $R_f=1 \text{ M}\Omega$ ) and an IA are used to measure the differential change in the capacitances  $C_1$  and  $C_2$  due to TM motion along  $x$ . A multi-feedback band-pass filter after the IA serves as an anti-aliasing filter and adds extra gain to minimize ADC quantization noise. The components of the design are chosen such that they have space qualified equivalent versions. Actuation signals are applied at  $\sim 100 \text{ Hz}$  through a DAC and a band-pass filter.  $R_a=1 \text{ M}\Omega$  and  $C_a=1 \text{ nF}$  decouple the sensing and actuating signals.

The TM sensing bias is applied at  $f_0 = 100 \text{ kHz}$  using the injection electrodes, which induce an oscillating voltage in the TM,  $V_{\text{TM}}$ , of about one tenth of the voltage applied to the electrodes. The two charge amplifiers at opposite faces of the TM sense the capacitances between the TM and the sensing electrodes. The outputs for each arm are (at 100 kHz)  $V_i = \frac{C_i}{C_f} V_{\text{TM}}$  ( $i=1,2$ ) where  $C_f$  is the feedback capacitor in the charge amplifier that defines the gain and using a parallel plate approximation,  $C_i = \epsilon_0 \frac{A}{d \pm x}$  where  $A$ ,  $d$  and  $x$  are the area of the sensing electrode, the gap between the TM and the electrode, and TM motion, respectively. The  $\pm$  symbol indicates that the change in the capacitance is anti-symmetric: TM motion in one direction causes an increase in  $C_1$  and a decrease in  $C_2$  and vice versa. The small changes in the TM position are encoded in the differential signal, which is obtained using an instrumentation amplifier (IA). The output of the IA is band-pass



filtered with a center frequency of 100 kHz and sampled with an analog-to-digital converter (ADC). The amplitude and phase of the 100 kHz signal is obtained after I/Q demodulation. The amplitude is proportional to the TM motion

$$\Delta V \simeq 2 \frac{GV_{\text{TM}}}{C_f} \frac{C_0}{d} \Delta x \quad (1)$$

where  $G = 40$  includes the gain of the IA and of the band-pass filter at 100 kHz.  $C_0$  is the capacitance between the TM and the electrode for  $x = 0$ . The most critical parts of the electronics are the charge amplifiers. For the values given in Fig. 11, the noise levels at 100 kHz referred to the input of the IA are  $51 \text{ nV/Hz}^{1/2}$  and are dominated by the charge amplifier stages (IA, BPF and ADC noise levels are negligible). The equivalent position sensing noise is readily calculated by considering the position sensitivity

$$\frac{1}{G} \frac{d\Delta V}{dx} \simeq 2 \frac{C_0}{d} \frac{V_{\text{TM}}}{C_f} \quad (2)$$

For  $C_0 = 3.9 \text{ pF}$  (capacitance in the most sensitive axis,  $x$ -direction),  $d = 1 \text{ mm}$ ,  $V_{\text{TM}} = 0.5 \text{ V}$  and  $C_f = 10 \text{ pF}$ , it is  $390 \text{ V/m}$ , which yields a noise equivalent position of  $0.13 \text{ nm/Hz}^{1/2}$ , i.e. well below the  $1 \text{ nm/Hz}^{1/2}$  goal. In terms of angular sensitivity this is equivalent to  $\sim 50 \text{ nrad/Hz}^{1/2}$ . Another source of error is due to common mode rejection (CMR) limitations and, more importantly, their fluctuations at the mHz frequency due to temperature variations. In this case, CMR fluctuations are dominated by the gain mismatch between the two charge amplifiers. The induced error in the TM position is  $\delta x = d\alpha_{C_f} \delta T$  where  $\alpha_{C_f}$  is the temperature coefficient of  $C_f$  and  $\delta T$  is the temperature fluctuation. This implies that the temperature coefficient has to be at the ppm/K level for  $1 \text{ K/Hz}^{1/2}$  temperature stability.

The experimental results for a single degree-of-freedom electronics prototype are shown in Fig. 12. The upper plot shows the ASD for a 6-hour measurement. The conversion to position noise has been done assuming  $V_{\text{TM}} = 0.5 \text{ V}$ . The noise levels for  $f > 20 \text{ mHz}$  are  $0.5 \text{ nm/Hz}^{1/2}$ , i.e., a factor  $\sim 4$  higher than the theoretical value, yet below  $1 \text{ nm/Hz}^{1/2}$ . For  $f < 20 \text{ mHz}$ , the noise levels increase due to temperature fluctuations and exhibit a plateau at  $3 \text{ nm/Hz}^{1/2}$  between  $0.1 \text{ mHz}$  and  $3 \text{ mHz}$ . The plot on the bottom shows the equivalent position changes when injecting temperature changes. The temperature coefficient is  $3.8 \text{ nm/K}$  ( $3.8 \text{ ppm/K}$  for  $d = 1 \text{ mm}$ ). The temperature sensitivity of the charge amplifiers can be further reduced by selecting matching capacitors  $C_f$ .

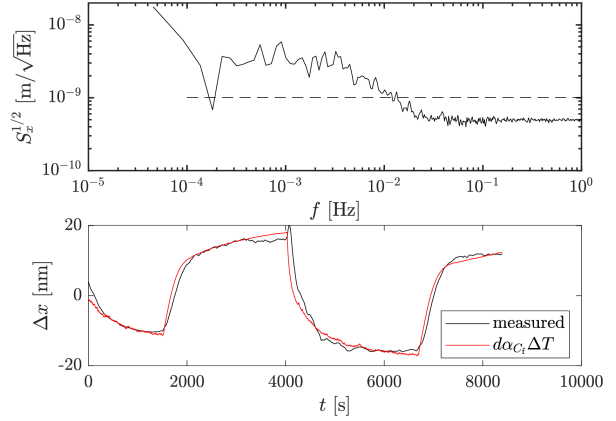


**Fig. 12** Top: sensing electronics noise in  $\text{m/Hz}^{1/2}$  (assuming  $V_{\text{TM}} = 0.5 \text{ V}$ ). Bottom: measured temperature coefficient. The best fit value is  $3.8 \text{ nm/K}$ . Both measurements are taken with fixed capacitors simulating the TM capacitances.

### 3.2 Electrostatic actuation

Electrostatic actuation is needed to keep the TM centered in the EH. The performance of such actuation is especially important in non-drag compensated mode since the applied electrostatic force is the signal used to derive the non-inertial forces acting on the spacecraft. The electrostatic forces are applied to the sensing electrodes at lower frequencies (50-300 Hz) to avoid interfering with the 100 kHz sensing signal. The circuit for the actuating signals is rather simple—see Fig. 11: a digital-to-analog converter (DAC) with a high-stability voltage reference and an active band-pass filter with gain. However, the requirements are stringent. The force on the TM for a single electrode is  $F \simeq \frac{1}{2} \frac{C_0}{d} V_{\text{act}}^2$  where  $V_{\text{act}}$  is the actuation signal at  $\sim 100 \text{ Hz}$ . In acceleration mode, the electrostatic force on the TM must be equal to the drag on the spacecraft to avoid a collision between them. At an altitude of 500 km, the drag on a GRACE-like spacecraft is about  $3 \times 10^{-7} \text{ m/s}^2$  (Mehta et al 2017), which requires an applied voltage of  $V_{\text{act}} \simeq 12 \text{ V}$  with stability requirements at the mHz band and at  $2f_{\text{act}}$  below  $10^{-6} \text{ 1/Hz}^{1/2}$ . At  $f_{\text{act}}$  the requirement is about  $20 \mu\text{V/Hz}^{1/2}$ . The stability at  $f_{\text{act}}$  and  $2f_{\text{act}}$  is not a problem for the actuator circuit. However, the requirement in the mHz band is challenging and, at a minimum, depends on the quality of the voltage reference of the DAC. Ultra-stable voltage references are available at the  $10^{-6} \text{ 1/Hz}^{1/2}$  level (Halloin et al 2013). The requirement at lower altitudes, e.g., 350 km is more demanding (Montenbruck and Gill 2000), which means  $10^{-12} \text{ m/s}^2/\text{Hz}^{1/2}$  noise levels cannot be reached unless a drag-free scheme is considered.

#### 4 Acceleration Noise Performance

A detailed acceleration noise model for the S-GRS has been developed based on two operational scenarios: non-drag-compensated at an orbit altitude of 500 km (similar to GRACE and GRACE-FO), and drag-compensated at an altitude of 350 km. The former and latter cases represent the worst and best realistic operational scenarios in terms of gravity recovery sensitivity. The model accounts for roughly 30 different noise sources that are relevant at acceleration noise levels below  $10^{-12} \text{ m/s}^2/\text{Hz}^{1/2}$  (Gerardi et al 2014). This model is based on both torsion pendulum experiments, flight experiments performed on the LPF mission (Armano et al 2018b) and measurements of the GRACE environment in orbit. The UF torsion pendulum, equipped with a LISA-like GRS, shown in Figure 4, has a demonstrated force noise performance below  $1 \text{ pN}/\text{Hz}^{1/2}$  at around 1 mHz acting on lightweight test mass in one degree-of-freedom (Ciani et al 2017).

Using the developed acceleration noise models and a spacecraft environment equivalent to that of GRACE-FO, Figure 13(a) shows the acceleration noise performance of the simplified GRS if operated on a drag-free platform at 350 km. Figure 13(b) shows the equivalent performance in a GRACE-like mission at 500 km with no drag-compensation. The performance of the S-GRS is expected to be roughly 40 times better than the GRACE accelerometers in the same mission configuration. If the sensor were operated on a drag-compensated platform, its performance would improve by an additional factor of 8 to about  $7 \times 10^{-13} \text{ m/s}^2/\text{Hz}^{1/2}$  around 1 mHz.

The bold lines in Figure 13 indicate the acceleration noise budget for the S-GRS in the two orbital environments. These curves have been used to evaluate the gravity recovery capability of the S-GRS in Section 4 over the frequency band of 0.1 mHz up to 0.1 Hz.

The ASD of the acceleration noise,  $S_a^{1/2}$ , in the drag-free environment can be described by the following function of frequency

$$S_a^{1/2} = 4 \times 10^{-13} \text{ m/s}^2/\text{Hz}^{1/2}$$

$$\sqrt{1 + \left(\frac{700 \mu\text{Hz}}{f}\right)^2 + \left(\frac{300 \mu\text{Hz}}{f}\right)^2}. \quad (3)$$

For the non-drag-compensated 500 km environment, the equivalent function describing the acceleration noise performance is

$$S_a^{1/2} = 5 \times 10^{-13} \sqrt{1 + \left(\frac{1 \text{ Hz}}{f}\right)^{2/3}} \text{ m/s}^2/\text{Hz}^{1/2} \quad (4)$$

The individual terms for the S-GRS noise model are grouped into six categories: stiffness, magnetic, thermal, Brownian, electrostatic, and actuation (Gerardi

et al 2014). Stiffness describes the coupling between the relative motion of spacecraft and TM and force gradients to produce an acceleration. Magnetic forces arise through the interaction of the bulk material of the TM with the magnetic field at the TM, comprising contributions from the Earth field and spacecraft components. Fluctuating temperatures and thermal gradients in the S-GRS create TM acceleration noise, through residual gas, radiation pressure and outgassing. Brownian noise is caused by random impacts of the residual gas molecules inside the vacuum chamber on the TM. Electrostatic forces produced by the variation of surface potentials and charge build-up on and around the TM create unwanted accelerations. Finally, noisy forces needed to control the TM position contribute to the total acceleration noise either directly in the sensitive axis or by cross-talk from orthogonal degrees-of-freedom. A calculation of each of these noise sources is included in Figure 13, as colored traces and the best estimate of the total acceleration noise is shown by the thin black curve. Actuation noise is not included in Figure 13(a) because test mass actuation along the sensitive axis of the instrument is not required in a drag free configuration. In Figure 13(b), the combined thermal, magnetic, Brownian and electrical effects are identical to the drag free case and are shown as the gray curve. The actuation noise and stiffness contributions in this mode are significantly higher because of the need to control the test mass position electrostatically and are therefore plotted explicitly. Also shown in Figures 13(a) and 13(b) are the displacement measurement noise curves for the LRI and S-GRS capacitive readout, twice differentiated to convert them to acceleration noise. Note that since LRI and S-GRS noise spectra are quite similar, neither one dominates the overall gravity recovery sensitivity.

##### 4.1 Detailed Noise Simulations

In the following sections we summarize the calculations of the major noise sources contributing to the acceleration noise budget of the S-GRS.

*Thermal Effects* Thermal acceleration noise effects in the S-GRS are driven by the fluctuation in temperature gradients across the TM. There are three physical sources of thermal gradient-induced noise: the radiometer effect, in which the residual gas in the gaps between the TM and EH has different pressure on opposite sides of the TM. Radiation pressure caused by the difference in energy of photons emitted by the hot and cold sides of the TM and EH, and the difference in temperature-dependent outgassing rates between hot and cold surfaces. Radiation pressure is well described

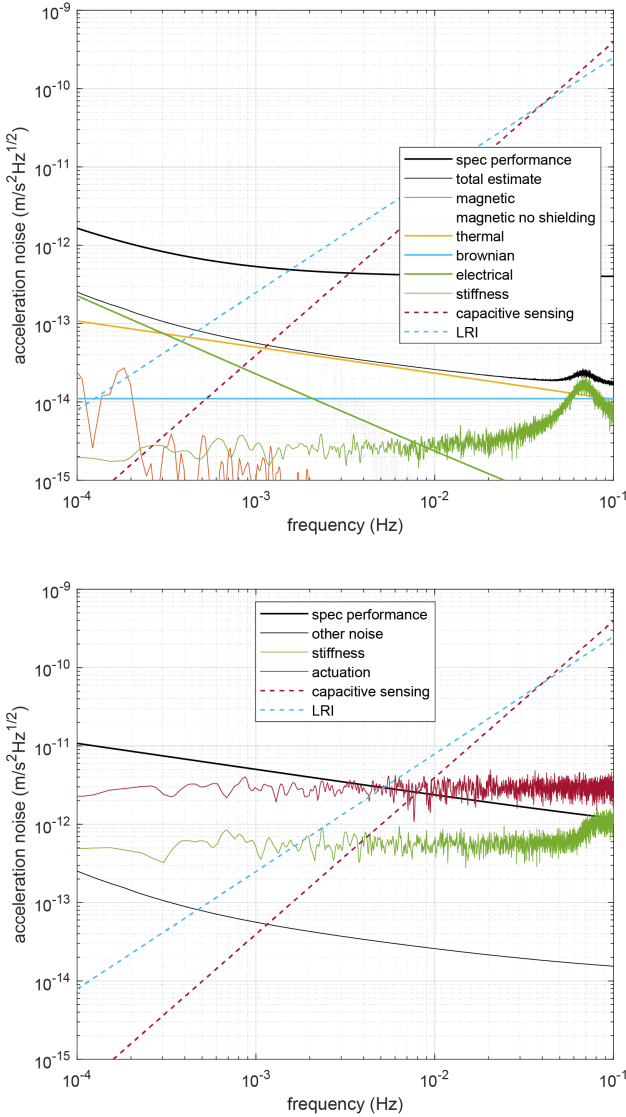


**Fig. 13** Acceleration noise estimate for the simplified GRS, operated on a drag-compensated platform at 350 km altitude (top) and operated on a GRACE-like spacecraft at 500 km (bottom), based on the measured GRACE-FO flight acceleration environment.

by analytical and geometrical expressions adapted from those derived for LISA and LPF (Carbone et al 2007). Both radiometer and outgassing effects depend on the geometry-dependent conductances of the EH. Because of this, the effects are simulated with the numerical analysis software MolFlow (Kersevan and Pons 2009). Using a simplified geometry of the TM and inner EH, the force per unit temperature gradient is determined by applying temperatures to the EH faces and calculating the pressure difference on the TM faces. Assuming water is the dominant outgassing species, an operational temperature of 293 K and a residual gas pres-

sure of  $10^{-5}$  Pa, temperature-gradient coupling parameters can be calculated for all three effects. To calculate the expected TM acceleration noise assumptions must be made about the stability of the temperature gradient across the EH. Data from the GRACE-FO mission, show that the temperature gradient stability at the accelerometer instrument is better than  $5 \text{ mK/Hz}^{1/2}$  at 1 mHz. Assuming a performance at this level for the S-GRS gives an upper limit of  $0.05 \text{ pm/s}^2/\text{Hz}^{1/2}$  for thermal effects at 1 mHz. A frequency dependence of  $f^{-1/2}$  is assumed.

*Gravitational Effects* The mass distribution on-board the spacecraft will produce a residual gravitational force and force gradient at the TM. The resulting acceleration of the TM is likely to be small compared to the drag on the spacecraft so that in non-drag free mode the acceleration is a small fraction of the actuation force. In a drag compensated mode of operation however, a continuous acceleration of the TM along the line of sight between spacecraft may eventually affect the inter-spacecraft laser metrology and require corrective maneuvers. This constraint will enforce some level of gravitational balancing on the spacecraft system. The LISA Pathfinder mission demonstrated the ability to compensate TM accelerations at the sub- $\text{pm/s}^2$  level (Armano et al (2016) but S-GRS performance likely does not require such fidelity.

In order to estimate the residual gravitational force on the TM, a mapping of components from a geometrical model of the GRACE-FO spacecraft was analyzed to estimate the volume and center of mass of each component, the S-GRS CAD design was also broken down into 127 mass elements. The gravitational force on the TM due to each component and S-GRS mass element was calculated resulting in a net residual dc acceleration on the order of  $30 \text{ nm/s}^2$ . This level of acceleration would result in an accumulated length change in the inter spacecraft distance of around 10 km in 10 days but could be mitigated by better gravitational balancing, station-keeping, or compensation by electrostatic actuation of the TM. The gravitational force also produces a force gradient at the TM of  $13.5 \text{ nN/m}$  in the initial estimate. This is an important contribution to the total stiffness of the TM. In band fluctuations of the gravitational force due to thermal distortion of the spacecraft were calculated and found to be negligible. This preliminary calculation provides only an order of magnitude estimation of the gravitational effects given that a flight platform for the S-GRS has not been defined.

*Magnetic Effects* The magnetic force  $F_{B,x}$  on the TM along the free-falling  $x$ -axis can be written as

$$F_{B,x} = \left( \frac{\chi_{\text{TM}} L_{\text{TM}}^3}{\mu_0} \mathbf{B} + \mathbf{M} \right) \cdot \nabla B_x, \quad (5)$$

where  $\mathbf{M}$  is the remnant magnetization of the TM,  $\chi_{\text{TM}}$  is the magnetic susceptibility,  $L_{\text{TM}}$  is the length of the TM side, and  $\mathbf{B}$  is the magnetic field at the TM. The remnant magnetization  $M$  of the gold platinum TM is expected to be around  $10^{-9} \text{ A m}^2$ , while the susceptibility  $\chi$  is around  $10^{-5}$ . The magnetic field at the TM originates from components on-board the spacecraft, and from Earth. The field gradient is dominated by the on-board component. The time-varying field at the spacecraft due to its motion through the Earth field, coupled with the static local field gradient gives rise to a magnetic force signal at harmonics of the orbital frequency. Stochastic noise in  $F_{B,x}$  arises from the coupling between the noise in the field gradient due to spacecraft equipment and the rms Earth field.

In order to estimate the magnitude of the magnetic effects, a magnetic map of the spacecraft has been created, similar to the gravitational analysis described above. Each spacecraft component is represented as a magnetic dipole at a position determined from a spacecraft geometrical model. The magnitude of the dipole is assigned to each element of the spacecraft equipment based on published measurements made on similar components of the LPF mission (Martin 2015). A simulation was developed, assigning each dipole a uniformly distributed random direction and calculating the field and gradient at the TM. 10,000 field realizations were calculated, which resulted in a local field magnitude of  $\pm 0.5 \mu\text{T}$  and a gradient of  $\pm 2.7 \mu\text{T/m}$  ( $1\sigma$ ). This is likely to be an optimistic estimate based on the simplicity of the geometry used. Given that the LISA Pathfinder gradient requirement was  $5 \mu\text{T/m}$  with stringent magnetic cleanliness requirements we assume a worst case gradient of  $500 \mu\text{T/m}$  in our acceleration noise calculations. The Earth field is measured on-board by GRACE-FO. The along track component of the field has a peak-to-peak amplitude of around  $55 \mu\text{T}$ . Combining these assumptions in Equation (5) results in the faint curve in Figure 13(a) which dominates the acceleration noise budget and motivates the inclusion of a magnetic shield within the S-GRS.

Initial estimates using a realistic geometry simulated in the COMSOL simulation toolkit indicate the magnetic shield will reduce the field and gradient at the TM by up to a factor 100 leading to an acceleration noise contribution represented by the red curve in Figure 13(a), suppressed by a factor  $10^4$  compared to the unshielded case. Incorporating a magnetic shield therefore relaxes significantly the magnetic cleanliness

requirements compared to LISA Pathfinder making it easier to accommodate the S-GRS as a secondary payload or on a spacecraft requiring an electrical thruster for drag compensation.

*Other acceleration noise sources* Electrostatic interactions between the charged TM and electric fields in the EH result in forces on the TM. Both the stray electric field and the charge build up on the TM are noisy resulting in an acceleration noise. The effect has been well studied in the context of the LISA mission Sumner et al (2020). Applying geometric scaling factors to those model predictions to account for the reduction in size of the S-GRS TM and gaps, and assuming a well-performing CMS, we expect a noise of around  $20 \text{ fm/s}^2/\text{Hz}^{1/2}$ . This level assumes continuous TM charge control using photoemission from UV light. In this case, the acceleration noise is dominated by the discharging current shot noise with a  $1/f$  shape and a magnitude that is expected to be similar to that expected for LISA. Assuming a worst case of uncompensated stray electric fields in the S-GRS leads to the green curve of Figure 13(a).

Electrostatic actuation forces applied to control the TM will introduce force noise through the imperfect stability of the voltages applied to actuation electrodes in a non drag-compensated mode of operation. The expected relative voltage stability for actuation voltages is around  $5 \times 10^{-6}$  resulting in a force noise of  $10 \times 10^{-6}$  of the applied actuation force. The magnitude of this effect is calculated from the control and actuation simulations described in Section 5 below. In a non-drag compensated operational mode, this is limiting contributor to the S-GRS acceleration noise performance shown by the dark red line in Figure 13(b).

As well as force noise, the electrostatic force needed to control the test mass position creates a significant force gradient. From the electrostatic control simulations, the commanded voltages on the electrodes produce a force gradient of  $3 \times 10^{-4} \text{ N/m}$ , while for a drag-compensated mode, the effect is reduced to around  $10^{-6} \text{ N/m}$ , contributed by the gravitational forces and the electrostatic sensing bias of the TM. Coupling these gradient values with the relative motion of the TM and SC shown in Figure 15 produces the light green traces of Figure 13(a) and (b).

## 4.2 Mission Architecture Considerations

Like previous Earth geodesy missions (and space gravitational wave interferometers), the proposed concept that includes the S-GRS, LRI, GPS receiver, and spacecraft forms a single “instrument”. The performance of

**Table 1** Required environmental parameters for the S-GRS

Quantity	Value
S/C-to-TM jitter (drag-comp.)	50 nm/Hz <sup>1/2</sup>
S/C-to-TM jitter (non-drag-comp.)	2 $\mu$ m/Hz <sup>1/2</sup>
Magnetic field at the TM	100 $\mu$ T
Magnetic field fluctuation at the TM	2 $\mu$ T/Hz <sup>1/2</sup>
Magnetic field gradient at the TM	20 $\mu$ T/m
Mag. field gradient fluctuation at TM	0.5 $\mu$ T/mHz <sup>1/2</sup>
Mean temperature at the TM	293 K
Temperature fluctuations across EH	5 mK/Hz <sup>1/2</sup>
Temperature fluctuations near TM	1 K/Hz <sup>1/2</sup>
Pressure around the TM	10 $\mu$ Pa

this instrument is directly tied to its attitude and possible drag-compensation control performance; as well as the thermal, electromagnetic, and gravitational environment provided for the S-GRS and LRI. Therefore, to maximize scientific performance, both the instrument and spacecraft platform must be considered. A spacecraft environment equivalent to that of GRACE-FO is assumed for the performance model described in the previous section. While the GRACE spacecraft busses provided a reasonably benign environment in low Earth orbit, no extreme measures were taken to control temperature, gravity and electromagnetics, like on the LPF spacecraft. Nevertheless, the S-GRS in the GRACE environment provides significant improvement. The mitigation steps taken in the S-GRS design include a small mu-metal magnetic shield surrounding the EH and the vacuum enclosure (see Figure 3). Including these measures, the key environmental parameters needed to achieve the stated performance are listed in Table 1.

The performance of the instrument in terms of gravity recovery accuracy is also closely tied to orbit selection and the number of orbits (satellite pairs). The number of pairs of satellites that is financially viable depends on the launch mass of each spacecraft and therefore the SWaP of the S-GRS and LRI. Finally, mission lifetime and orbit altitude also depend on whether a drag-compensated platform is chosen.

The estimated mass of the S-GRS Head and electronics unit is  $\sim 8$  kg and  $\sim 5$  kg respectively. The power consumption of the S-GRS electronics unit is  $\sim 20$  W. The total mass of the GRACE-FO LRI units per spacecraft is 25 kg, and the nominal power consumption is 35 W. The sum of these results is a mass of  $\sim 38$  kg and power consumption of  $\sim 55$  W. These values already put the mass and power budget of the S-GRS and LRI within levels typically accommodated on ESPA-class microsatellites satellites, whose size and mass are 1/3 of the GRACE-FO spacecraft.

## 5 S-GRS and Drag-compensation Control

In both drag compensated and non-drag compensated modes of operation, the TM position must be controlled, either by actuation of the spacecraft with micro-Newton thrusters or by electrostatic actuation of the TM. The residual jitter of the TM position relative to the spacecraft drives the stiffness contribution to acceleration noise budget and, in the non-drag compensated case, the noisy TM actuation force is an important noise contribution. We have developed a control system for both modes of operation and here we show the performance in the critical  $x$  (SC-SC) direction.

The performance is evaluated through a numerical simulation that uses realistic sensing noise, actuation noise, and spacecraft environment. The control of the spacecraft is simulated in both the non-drag-compensated and drag-compensated case. In both cases, a state space representation of a simple equation of motion for the linear satellite dynamics is used.

$$\ddot{x} = a_{SC} + a_{TM} + \frac{K}{m_{TM}}x \quad (6)$$

where  $a_{SC}$  is the environmental disturbance on the spacecraft,  $a_{TM}$  is the direct TM force noise,  $K$  is the stiffness,  $m_{TM}$  is the mass of the TM and  $x$  is the relative position of the TM with respect to the SC. The position sensor noise and applied actuation forces are accounted for when applying this equation in the simulation.

The controls simulation is done using MATLAB and Simulink to simulate around one day of data. For the non-drag compensated case at 500 km altitude, the spacecraft acceleration noise is taken from previously recorded GRACE-FO Level-1B accelerometer data along the  $x$ -direction, which measures the relative acceleration between the test mass and spacecraft and we assume this measurement is dominated by the spacecraft acceleration signal. At 350 km we assume the along-track disturbance is 10 times greater. The position sensor noise in both cases is modeled as a Gaussian white noise with a level of 1 nm/Hz<sup>1/2</sup> while the direct forces on the test mass, excluding actuation are approximated by a white noise of 0.2 pN/Hz<sup>1/2</sup>. A spring constant of 1  $\mu$ N/m, is used for the drag-compensated case in which electrostatic stiffness from TM actuation forces will be small, in a non-drag compensated case where large voltages are applied to sensor electrodes, a value of 310  $\mu$ N/m is used. This figure was calculated from the commanded voltages output from the simulation described below, iterating from an initial value of 100  $\mu$ N/m for the stiffness.

The feedback control block diagram is shown in Figure 14 indicating the modelled disturbances, sensing and actuation noises. In order to reduce stiffness con-



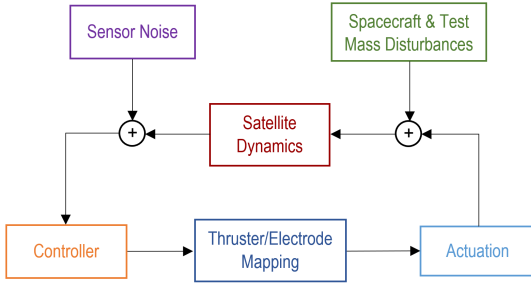


Fig. 14 Control loop block diagram.

tributions to the acceleration noise budget, the aim of the controller in both control schemes is to reduce the in-band motion of the test mass to below  $50 \text{ nm/Hz}^{1/2}$  for drag-compensated and below  $2 \mu\text{m/Hz}^{1/2}$  for non-drag-compensated. In both cases, an H-infinity optimization method is employed to determine the control effort needed to stabilize the motion. This method allows for the disturbances and noise to be accounted for in the control algorithm by using a Multi-Input Multi-Output system and indicating which error outputs are to be kept small. Using the function `hinfscn` in MATLAB, we minimized the position readout and velocity jitter.

The thruster model for the drag-compensated simulation is based on cold-gas thrusters used in the Gaia, Microscope and LISA Pathfinder missions Armano et al (2019). Our model is capable of simulating 6-dof SC control although here we present only the results for the critical  $x$  direction. Similar to the Grace thruster system, four thrusters actuate each degree of freedom,  $(x, y, z)$ , linear thrust is achieved by actuating thrusters on the same face of the spacecraft, torques are obtained commanding thrust to opposite pairs. The thrusters are positioned so that translational thrust produces no moment and rotations produce no net force. Once the command to each individual thruster has been calculated, the constraints of a cold gas thruster model are applied. A resolution of  $0.1 \mu\text{N}$  and range of 2 to  $1000 \mu\text{N}$  is used, with a time response of 250 ms to 63% of the commanded thrust level. A thrust noise of  $0.17 \mu\text{N/Hz}^{1/2}$  is also added in this step. The maximum thrust used here is extended beyond the capability of the system included on LISA Pathfinder. It remains to be investigated whether there are technical barriers to achieving this thrust level, however, a number of other micro-thruster technologies are under development which may address the required thrust range and resolution.

For the non-drag-compensated case, the S-GRS electrodes are utilized as actuators on the test mass. Commanded forces and torques are converted to electrode voltages using a simple electrostatic model. Assuming a maximum applied voltage of 15 V with 16-bits of resolu-

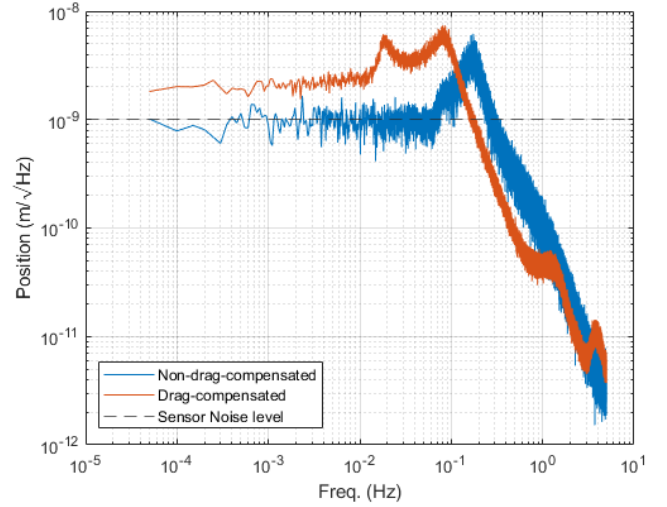
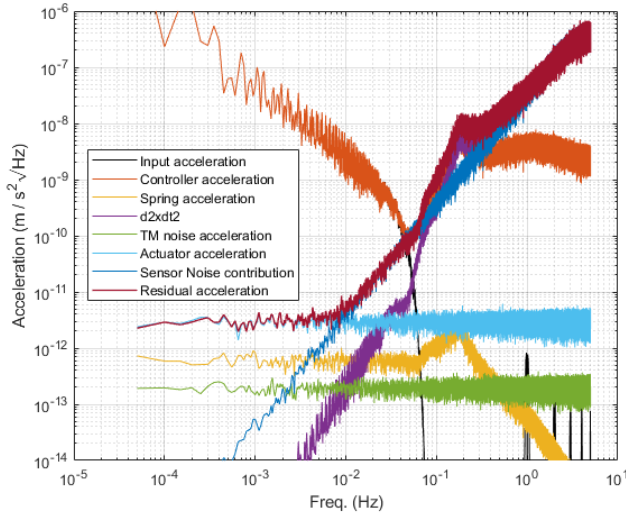


Fig. 15 One degree-of-freedom in-loop position ASD for drag-compensated and non-drag-compensated cases.

tion, the maximum force that can be applied to the TM in our model is about  $0.4 \mu\text{N}$  with resolution of  $0.1 \text{ fN}$ . The ASD of the voltage noise is calculated as 5 ppm of the rms commanded voltage on each electrode. This noise is added to the commanded before calculating the resulting force on the test mass.

The results of the  $x$ -axis position simulation for drag-compensated and non-drag compensated cases are shown in Figure 15. The drag-compensated simulation results show that the larger input noise from the 350 km orbit is causing this case is gain limited, but still within the  $50 \text{ nm/Hz}^{1/2}$  jitter requirements. The non-drag-compensated simulation shows that the in-loop position measurement is at a level below the measurement noise successfully suppressing stiffness contributions to the acceleration noise budget. The controller performs optimally so that the sensor noise level is the limiting factor and there is no wasted control effort. They both make a negligible contribution to the acceleration noise budget.

Further analyzing the non-drag compensated case, we can confirm the limiting sensitivity of the S-GRS from the simulated data. In this mode of operation the spacecraft acceleration would be determined from the S-GRS measurements and applied control forces. Figure 16 shows the ASD of various sources of apparent TM acceleration in the simulation. The red curve shows the input SC acceleration to the simulation. After subtracting the commanded control forces, the residual acceleration is given by the dark red curve. This represents the performance limit of the S-GRS at  $3 \times 10^{-12} \text{ m/s}^2\text{Hz}^{1/2}$  and is limited by the actuation noise (light blue curve) and position sensor noise (dark blue curve). Also shown are the sub-dominant contributions of stiff-



**Fig. 16** Residual acceleration for the non-drag-compensated case.

ness (yellow), direct TM forces (green) and in-loop TM motion estimate (purple).

## 6 Conclusions and Outlook

We have developed a novel simplified gravitational reference sensor optimized for future Earth geodesy missions. This sensor is a scaled-down version of the flight LPF GRS with reduced complexity. The performance is roughly 40 times better than that of the accelerometers flown on GRACE and GRACE-FO when operated on a non-drag-compensated spacecraft in a 500 km altitude Earth orbit. When operated on a drag-compensated spacecraft the performance improvement is a factor of 500. This is achieved by eliminating the small grounding wire used in prior accelerometers and instead using a UV photoemission-based TM charge control scheme. In addition to eliminating the noise associated with the grounding wire, this also allows for a larger TM and a larger TM-to-electrode housing gap. We described the mechanical and electrical design of the S-GRS and provided details of our performance assessment, which is based on models validated by LPF and torsion pendulum experiments, and used flight environment data from GRACE-FO. Gravity recovery simulations reveal that the S-GRS noise and the GRACE-FO LRI noise contribute equally to the gravity recovery sensitivity of a mission that utilizes both. Therefore, neither the S-GRS nor the LRI would limit measurement sensitivity.

A team led by the University of Florida, in collaboration with Caltech/JPL and Ball Aerospace is advancing the technology readiness level of the S-GRS. Currently considered TRL 3-5, depending on the com-

ponent, we plan to reach TRL 5-6 in three years and flight readiness by the mid-to-late 2020's.

## A Appendix

High fidelity numerical simulations relying on the same software suite used to process GRACE and GRACE-FO data at JPL were run to quantify performance in Figures 1 and 2. The simulations consist of a truth run to create a set of synthetic satellite observations based on a realistic flight environment, followed by a nominal run where the truth measurements are perturbed in some way. The error in the recovered gravity field due to this perturbation is then quantified via a large linear least squares estimation process, as is commonly used in the GRACE and GRACE-FO data processing. Force models used in the truth and nominal runs are given in Table 2 when temporal aliasing error is included in the simulation. When only measurement system error is considered, the nominal models in Table 2 are set equivalent to the truth models, so there is no perturbation among the model. The simulation timeframe is January 1-29, 2006. The gravity estimation process is a 2-step process, where in the first step, a set of “local” parameters are estimated using the tracking data to converge to a best fitting orbit. These parameters consist of daily position and velocity of each spacecraft, daily accelerometer scale factors and biases, and range-rate biases, drifts, and one cycle per revolution each orbital revolution. In the second step of the gravity estimation process, these same parameters are again adjusted along with a 29-day mean gravity field expressed to spherical harmonic degree and order 180.

**Table 2** Force Models used in Numerical Simulations

Measurement	Truth Model	Nominal Model
Static Gravity Field	gif48	gif48
Ocean Tides	GOT4.8	FES2004
Nontidal Atmosphere and Ocean (AOD)	AOD RL05	AOerr + DEAL (Dobslaw et al 2016)
Hydrology + Ice	ESA Earth System Model	N/A

Measurement system errors ingested into the simulation process rely largely on heritage information from GRACE-FO. Orbit error is introduced by adding 1 cm white noise in all 3-axes with a 5-minute sampling time. Attitude Error is derived using the difference of two competing data products used to define the GRACE-FO attitude. For pitch and yaw, the difference between an attitude solution that combines star tracker and

IMU data (as in the GRACE-FO v04 SCA1B data product) with star tracker and laser steering mirror data (from the LRI) is used to define the error (Goswami et al 2021). Since the laser steering mirror is insensitive to roll variations, roll error is defined as the difference between an attitude solution that uses only star tracker data with one that uses both star tracker and IMU data. LRI error is derived from GRACE-FO flight data (Abich et al 2019), where laser frequency noise dominates high frequencies and tilt-to-length coupling error dominates lower frequencies (Wegener et al 2020). The LRI error curves with ‘improved alignment’ assume the tilt-to-length coupling error is driven to zero via improved alignments relative to the center of mass of the spacecraft. The GRACE-FO accelerometer error is taken as the best estimate of performance prior to launch of GRACE-FO and is approximately a factor 3 better than the requirement discussed in (Kornfeld et al 2019). The S-GRS error is described in detail in Section 4.

## Acknowledgements

This work was supported by the NASA Earth Science Technology Office (ESTO) grant 80NSSC20K0324.

We thank Peter Bender for his insights into the benefits of improved accelerometry for future GRACE-like missions.

## References

- Abich K, Bogan C, Braxmaier C, Danzmann K, Kaufer M, Gohlke M, Koch A, Heinzl G, Herding M, Mahrtdt C, Müller V, Nicklaus K, Sanjuan J, Schütze D, Sheard B, Stede G, Voss K (2015) Grace-follow on laser ranging interferometer: German contribution. *Journal of Physics: Conference Series* 610:012,010, DOI 10.1088/1742-6596/610/1/012010
- Abich K, Abramovici A, Amparan B, Baatzsch A, Okiiro BB, Barr DC, Bize MP, Bogan C, Braxmaier C, Burke MJ, Clark KC, Dahl C, Dahl K, Danzmann K, Davis MA, de Vine G, Dickson JA, Dubovitsky S, Eckardt A, Ester T, Barranco GF, Flatscher R, Flechtner F, Folkner WM, Francis S, Gilbert MS, Gilles F, Gohlke M, Grossard N, Guenther B, Hager P, Hauden J, Heine F, Heinzl G, Herding M, Hinz M, Howell J, Katsumura M, Kaufer M, Klipstein W, Koch A, Kruger M, Larsen K, Lebeda A, Lebeda A, Leikert T, Liebe CC, Liu J, Lobmeyer L, Mahrtdt C, Mangoldt T, McKenzie K, Misfeldt M, Morton PR, Müller V, Murray AT, Nguyen DJ, Nicklaus K, Pierce R, Ravich JA, Reavis G, Reiche J, Sanjuan J, Schütze D, Seiter C, Shaddock D, Sheard B, Sileo M, Spero R, Spiers G, Stede G, Stephens M, Sutton A, Trinh J, Voss K, Wang D, Wang RT, Ware B, Wegener H, Windisch S, Woodruff C, Zender B, Zimmermann M (2019) In-orbit performance of the grace follow-on laser ranging interferometer. *Phys Rev Lett* 123:031,101, DOI 10.1103/PhysRevLett.123.031101, URL <https://link.aps.org/doi/10.1103/PhysRevLett.123.031101>
- Armano M, Audley H, Auger G, Baird J, Binetruy P, Born M, Bortoluzzi D, Brandt N, Bursi A, Caleno M, Cavalleri A, Cesarini A, Cruise M, Danzmann K, de Deus Silva M, Desiderio D, Piersanti E, Diepholz I, Dolesi R, Dunbar N, Ferraioli L, Ferroni V, Fitzsimons E, Flatscher R, Freschi M, Gallegos J, Marirrodiga CG, Gerndt R, Gesa L, Gibert F, Giardini D, Giusteri R, Grimaldi C, Grzymisch J, Harrison I, Heinzl G, Hewitson M, Hollington D, Hueller M, Huesler J, Inchauspé H, Jennrich O, Jetzer P, Johlander B, Karnesis N, Kaune B, Korsakova N, Killow C, Lloro I, Liu L, López-Zaragoza JP, Maarschalkerweerd R, Madden S, Mance D, Martín V, Martin-Polo L, Martino J, Martin-Porqueras F, Mateos I, McNamara PW, Mendes J, Mendes L, Moroni A, Nofrarias M, Paczkowski S, Perreux-Lloyd M, Petiteau A, Pivato P, Plagnol E, Prat P, Ragnit U, Ramos-Castro J, Reiche J, Perez JAR, Robertson D, Rozemeijer H, Rivas F, Russano G, Sarra P, Schleicher A, Slutsky J, Sopuerta CF, Sumner T, Texier D, Thorpe JI, Tomlinson R, Trenkel C, Vetrugno D, Vitale S, Wanner G, Ward H, Warren C, Wass PJ, Wealthy D, Weber WJ, Wittchen A, Zanoni C, Ziegler T, Zweifel P (2016) Constraints on LISA pathfinder’s self-gravity: design requirements, estimates and testing procedures. *Classical and Quantum Gravity* 33(23):235,015, DOI 10.1088/0264-9381/33/23/235015, URL <https://doi.org/10.1088/0264-9381/33/23/235015>
- Armano M, Audley H, Baird J, Binetruy P, Born M, Bortoluzzi D, Castelli E, Cavalleri A, Cesarini A, Cruise AM, Danzmann K, de Deus Silva M, Diepholz I, Dixon G, Dolesi R, Ferraioli L, Ferroni V, Fitzsimons ED, Freschi M, Gesa L, Giardini D, Gibert F, Giusteri R, Grimaldi C, Grzymisch J, Harrison I, Heinzl G, Hewitson M, Hollington D, Hoyland D, Hueller M, Inchauspé H, Jennrich O, Jetzer P, Karnesis N, Kaune B, Korsakova N, Killow CJ, Liu L, Lloro I, Lobo JA, López-Zaragoza JP, Maarschalkerweerd R, Mailland F, Mance D, Martín V, Martin-Polo L, Martin-Porqueras F, Martino J, Mateos I, McNamara PW, Mendes J, Mendes L, Meshkar N, Nofrarias M, Paczkowski S, Perreux-

- Lloyd M, Petiteau A, Pfeil M, Pivato P, Plagnol E, Ramos-Castro J, Reiche J, Robertson DI, Rivas F, Russano G, Santoruvo G, Sarra P, Shaul D, Slutsky J, Sopena CF, Sumner T, Texier D, Thorpe JI, Trenkel C, Vetrugno D, Vitale S, Wanner G, Ward H, Waschke S, Wass PJ, Weber WJ, Wissel L, Wittchen A, Zweifel P (2018a) Precision charge control for isolated free-falling test masses: Lisa pathfinder results. *Phys Rev D* 98:062,001, DOI 10.1103/PhysRevD.98.062001, URL <https://link.aps.org/doi/10.1103/PhysRevD.98.062001>
- Armano M, Audley H, Baird J, Binetruy P, Born M, Bortoluzzi D, Castelli E, Cavalleri A, Cesarini A, Cruise AM, Danzmann K, de Deus Silva M, Diepholz I, Dixon G, Dolesi R, Ferraioli L, Ferroni V, Fitzsimons ED, Freschi M, Gesa L, Gibert F, Giardini D, Giusteri R, Grimaldi C, Grzymisch J, Harrison I, Heinzel G, Hewitson M, Hollington D, Hoyland D, Hueller M, Inchauspé H, Jennrich O, Jetzer P, Karnesis N, Kaune B, Korsakova N, Killow CJ, Lobo JA, Lloro I, Liu L, López-Zaragoza JP, Maarschalk-erweerd R, Mance D, Meshksar N, Martín V, Martin-Polo L, Martino J, Martin-Porqueras F, Mateos I, McNamara PW, Mendes J, Mendes L, Nofrarias M, Paczkowski S, Perreux-Lloyd M, Petiteau A, Pivato P, Plagnol E, Ramos-Castro J, Reiche J, Robertson DI, Rivas F, Russano G, Slutsky J, Sopena CF, Sumner T, Texier D, Thorpe JI, Vetrugno D, Vitale S, Wanner G, Ward H, Wass PJ, Weber WJ, Wissel L, Wittchen A, Zweifel P (2018b) Beyond the required lisa free-fall performance: New lisa pathfinder results down to 20  $\mu$ Hz. *Phys Rev Lett* 120:061,101, DOI 10.1103/PhysRevLett.120.061101, URL <https://link.aps.org/doi/10.1103/PhysRevLett.120.061101>
- Armano M, Audley H, Baird J, Binetruy P, Born M, Bortoluzzi D, Castelli E, Cavalleri A, Cesarini A, Cruise AM, Danzmann K, de Deus Silva M, Diepholz I, Dixon G, Dolesi R, Ferraioli L, Ferroni V, Fitzsimons ED, Freschi M, Gesa L, Gibert F, Giardini D, Giusteri R, Grimaldi C, Grzymisch J, Harrison I, Heinzel G, Hewitson M, Hollington D, Hoyland D, Hueller M, Inchauspé H, Jennrich O, Jetzer P, Karnesis N, Kaune B, Korsakova N, Killow CJ, Lobo JA, Lloro I, Liu L, López-Zaragoza JP, Maarschalk-erweerd R, Mance D, Meshksar N, Martín V, Martin-Polo L, Martino J, Martin-Porqueras F, Mateos I, McNamara PW, Mendes J, Mendes L, Nofrarias M, Paczkowski S, Perreux-Lloyd M, Petiteau A, Pivato P, Plagnol E, Ramos-Castro J, Reiche J, Robertson DI, Rivas F, Russano G, Slutsky J, Sopena CF, Sumner T, Texier D, Thorpe JI, Vetrugno D, Vitale S, Wanner G, Ward H, Wass PJ, Weber WJ, Wissel L, Wittchen A, Zweifel P (2019) Lisa pathfinder micronewton cold gas thrusters: In-flight characterization. *Phys Rev D* 99:122,003, DOI 10.1103/PhysRevD.99.122003, URL <https://link.aps.org/doi/10.1103/PhysRevD.99.122003>
- Bortoluzzi D, Conklin JW, Zanoni C (2013) Prediction of the LISA-Pathfinder release mechanism in-flight performance. *Adv Space Res* 51:1145–1156, DOI 10.1016/j.asr.2012.11.001
- Bortoluzzi D, Armano M, Audley H, Auger G, Baird J, Binétruy P, Born M, Brandt N, Bursi A, Caleno M, Cavalleri A, Cesarini A, Conklin J, Cruise M, Danzmann K, Diepholz I, Dolesi R, Dunbar N, Ferraioli L, Ferroni V, Fitzsimons E, Freschi M, Slutsky J, Thorpe J (2016) Injection of a body into a geodesic: Lessons learnt from the lisa pathfinder case. In: 43rd Aerospace Mechanisms Symposium
- Carbone L, Cavalleri A, Ciani G, Dolesi R, Hueller M, Tombolato D, Vitale S, Weber WJ (2007) Thermal gradient-induced forces on geodesic reference masses for lisa. *Phys Rev D* 76:102,003, DOI 10.1103/PhysRevD.76.102003, URL <https://link.aps.org/doi/10.1103/PhysRevD.76.102003>
- Christophe B, Marque J, Foulon B (2010) In-orbit data verification of the accelerometers of the esa goce mission. In: SF2A-2010: Proceedings of the Annual meeting of the French Society of Astronomy and Astrophysics
- Ciani G (2008) Free-fall of lisa test masses: a new torsion pendulum to test translational acceleration. PhD thesis, Università degli studi di Trento
- Ciani G, Chilton A, Apple S, Olatunde T, Aitken M, Mueller G, Conklin JW (2017) A new torsion pendulum for gravitational reference sensor technology development. *Review of Scientific Instruments* 88(6):064,502, DOI 10.1063/1.4985543, URL <http://dx.doi.org/10.1063/1.4985543>
- Dahl C, Baatzsch A, Dehne M, Gilles F, Hager P, Herding M, Nicklaus K, Voss K, Abich K, Braxmaier C, Gohlke M, Guenther B, Sanjuan J, Zender B, Baranco GF, Göth A, Mahrdt C, Müller V, Schütze D, Stede G, Heinzel G (2017) Laser ranging interferometer on Grace follow-on. In: Cugny B, Karafolas N, Sodnik Z (eds) International Conference on Space Optics — ICSO 2016, International Society for Optics and Photonics, SPIE, vol 10562, pp 1133 – 1141, URL <https://doi.org/10.1117/12.2297705>
- Danzmann K, Rüdiger A (2003) Lisa technology - concept, status, prospects. *Classical and Quantum Gravity*, v20, S1-S9 (2003) 20, DOI 10.1088/0264-9381/20/10/301
- Daras I, Pail R (2017) Treatment of temporal aliasing effects in the context of next generation satellite gravimetry missions. *Journal of Geophysical*

- Research: Solid Earth 122(9):7343–7362, DOI <https://doi.org/10.1002/2017JB014250>, URL <https://agupubs.onlinelibrary.wiley.com/doi/abs/10.1002/2017JB014250>, <https://agupubs.onlinelibrary.wiley.com/doi/pdf/10.1002/2017JB014250>
- Dobslaw H, Bergmann-Wolf I, Forootan E, Dahle C, Mayer-Gürr T, Kusche J, Flechtner F (2016) Modeling of present-day atmosphere and ocean non-tidal de-aliasing errors for future gravity mission simulations. *Journal of Geodesy* 90, DOI 10.1007/s00190-015-0884-3
- Dolesi R, Bortoluzzi D, Bosetti P, Carbone L, Cavalleri A, Cristofolini I, DaLio M, Fontana G, Fontanari V, Foulon B, Hoyle CD, Hueller M, Nappo F, Sarra P, Shaul DNA, Sumner T, Weber WJ, Vitale S (2003) Gravitational sensor for LISA and its technology demonstration mission. *Classical and Quantum Gravity* 20(10):S99–S108, DOI 10.1088/0264-9381/20/10/312, URL <https://doi.org/10.1088/0264-9381/20/10/312>
- Drinkwater MR, Floberghagen R, Haagmans R, Muzi D, Popescu A (2003) GOCE: ESA's First Earth Explorer Core Mission, Springer Netherlands, Dordrecht, pp 419–432. DOI 10.1007/978-94-017-1333-7\_36, URL [https://doi.org/10.1007/978-94-017-1333-7\\_36](https://doi.org/10.1007/978-94-017-1333-7_36)
- Elsaka B, Raimondo JC, Brieden P, Reubelt T, Kusche J, Flechtner F, Pour S, Sneeuw N, Müller J (2013) Comparing seven candidate mission configurations for temporal gravity field retrieval through full-scale numerical simulation. *Journal of Geodesy* 88, DOI 10.1007/s00190-013-0665-9
- Everitt CWF, DeBra DB, Parkinson BW, Turneure JP, Conklin JW, Heifetz MI, Keiser GM, Silbergleit AS, Holmes T, Kolodziejczak J, et al (2011) Gravity probe b: Final results of a space experiment to test general relativity. *Physical Review Letters* 106(22), DOI 10.1103/physrevlett.106.221101, URL <http://dx.doi.org/10.1103/PhysRevLett.106.221101>
- Gerardi D, Allen G, Conklin JW, Sun KX, DeBra D, Buchman S, Gath P, Fichter W, Byer RL, Johann U (2014) Invited article: Advanced drag-free concepts for future space-based interferometers: acceleration noise performance. *Review of Scientific Instruments* 85(1):011,301, DOI 10.1063/1.4862199, URL <https://doi.org/10.1063/1.4862199>, <https://doi.org/10.1063/1.4862199>
- Ghobadi-Far K, Han SC, Weller S, Loomis BD, Luthcke SB, Mayer-Gürr T, Behzadpour S (2018) A transfer function between line-of-sight gravity difference and grace intersatellite ranging data and an application to hydrological surface mass variation. *Journal of Geophysical Research: Solid Earth* 123(10):9186–9201, DOI <https://doi.org/10.1029/2018JB016088>, URL <https://agupubs.onlinelibrary.wiley.com/doi/abs/10.1029/2018JB016088>, <https://agupubs.onlinelibrary.wiley.com/doi/pdf/10.1029/2018JB016088>
- Ghobadi-Far K, Han SC, McCullough CM, Wiese DN, Yuan DN, Landerer FW, Sauber J, Watkins MM (2020) Grace follow-on laser ranging interferometer measurements uniquely distinguish short-wavelength gravitational perturbations. *Geophysical Research Letters* 47(16):e2020GL089445, DOI <https://doi.org/10.1029/2020GL089445>, URL <https://agupubs.onlinelibrary.wiley.com/doi/abs/10.1029/2020GL089445>, e2020GL089445, <https://agupubs.onlinelibrary.wiley.com/doi/pdf/10.1029/2020GL089445>
- Goswami S, Francis SP, Bandikova T, Spero RE (2021) Analysis of grace follow-on laser ranging interferometer derived inter-satellite pointing angles. *IEEE Sensors Journal* 21(17):19,209–19,221, DOI 10.1109/jsen.2021.3090790, URL <http://dx.doi.org/10.1109/JSEN.2021.3090790>
- Halluin H, Prat P, Brossard J (2013) Long term characterization of voltage references. 1312.5101
- Han SC, Ghobadi-Far K, Yeo IY, McCullough CM, Lee E, Sauber J (2021a) Grace follow-on revealed bangladesh was flooded early in the 2020 monsoon season due to premature soil saturation. *Proceedings of the National Academy of Sciences* 118(47), DOI 10.1073/pnas.2109086118, URL <https://www.pnas.org/content/118/47/e2109086118>, <https://www.pnas.org/content/118/47/e2109086118.full.pdf>
- Han SC, Yeo IY, Khaki M, McCullough CM, Lee E, Sauber J (2021b) Novel along-track processing of grace follow-on laser ranging measurements found abrupt water storage increase and land subsidence during the 2021 march australian flooding. *Earth and Space Science* 8(11):e2021EA001941, DOI <https://doi.org/10.1029/2021EA001941>, URL <https://agupubs.onlinelibrary.wiley.com/doi/abs/10.1029/2021EA001941>, e2021EA001941, <https://agupubs.onlinelibrary.wiley.com/doi/pdf/10.1029/2021EA001941>
- Hauk M, Wiese DN (2020) New methods for linking science objectives to remote sensing observations: A concept study using single- and dual-pair satellite gravimetry architectures. *Earth and Space Science* 7(3):e2019EA000922, DOI <https://doi.org/10.1029/2019EA000922>, URL <https://agupubs.onlinelibrary.wiley.com/doi/abs/10.1029/2019EA000922>, e2019EA000922, <https://agupubs.onlinelibrary.wiley.com/doi/pdf/10.1029/2019EA000922>



- Inchauspé H, Olatunde T, Apple S, Parry S, Letson B, Turetta N, Mueller G, Wass P, Conklin J (2020) Numerical modeling and experimental demonstration of pulsed charge control for the space inertial sensor used in lisa. *Physical Review D* 102(4), DOI 10.1103/physrevd.102.042002, URL <http://dx.doi.org/10.1103/PhysRevD.102.042002>
- Josselin V, Touboul P, Kielbasa R (1999) Capacitive detection scheme for space accelerometers applications. *Sensors and Actuators A-physical* 78:92–98
- Kenyon SP, Letson B, Clark M, Olatunde T, Ritten L, Schindler J, Wass PJ, Conklin JW, Barke S, Mueller G, Sumner TJ (2021) A charge management system for gravitational reference sensors – design and instrument testing. In: 2021 IEEE Aerospace Conference (50100), pp 1–9, DOI 10.1109/AERO50100.2021.9438339
- Kersevan R, Pons JL (2009) Introduction to molflow+: New graphical processing unit-based monte carlo code for simulating molecular flows and for calculating angular coefficients in the compute unified device architecture environment. *Journal of Vacuum Science & Technology A* 27(4):1017–1023, DOI 10.1116/1.3153280, URL <https://doi.org/10.1116/1.3153280>, <https://doi.org/10.1116/1.3153280>
- Kornfeld RP, Arnold BW, Gross MA, Dahya NT, Klipstein WM, Gath PF, Bettadpur S (2019) Gracefo: The gravity recovery and climate experiment follow-on mission. *Journal of Spacecraft and Rockets* 56(3):931–951, DOI 10.2514/1.A34326, URL <https://doi.org/10.2514/1.A34326>, <https://doi.org/10.2514/1.A34326>
- Lotters J, Olthuis W, Veltink P, Bergveld P (1999) A sensitive differential capacitance to voltage converter for sensor applications. *IEEE Transactions on Instrumentation and Measurement* 48(1):89–96, DOI 10.1109/19.755066
- Martin M (2015) Design and assessment of a low-frequency magnetic measurement system for elisa. PhD thesis, Universitat Politècnica de Catalunya
- McNamara P, Antonucci F, Armano M, Audley H, Auger G, Benedetti M, Binetruy P, Bogenstahl J, Bortoluzzi D, Brandt N, Caleno M, Cavalleri A, Congedo G, Cruise M, Danzmann K, De Marchi F, Diaz-Aguilo M, Diepholz I, Dixon G, Dolesi R, Dumbbar N, Fauste J, Ferraioli L, Ferroni V, Fichter W, Fitzsimons E, Freschi M, García Marirrodriaga C, Gerndt R, Gesa L, Gibert F, Giardini D, Grimaldi C, Grynagier A, Guzmán F, Harrison I, Heinzel G, Hewitson M, Hollington D, Hoyland D, Hueller M, Huesler J, Jennrich O, Jetzer P, Johlander B, Karnešić N, Korsakova N, Killow C, Llamas X, Lloro I, Lobo A, Maarschalkerweerd R, Madden S, Mance D, Martin V, Mateos I, Mendes J, Mitchell E, Nicolodi D, Nofrarias M, Perreux-Lloyd M, Plagnol E, Prat P, Ramos-Castro J, Reiche J, Romera Perez JA, Robertson D, Rozemeijer H, Russano G, Schleicher A, Shaul D, Sopuerta CF, Sumner TJ, Taylor A, Texier D, Trenkel C, Tu HB, Vitale S, Wanner G, Ward H, Waschke S, Wass P, Wealthy D, Wen S, Weber W, Ziegler T, Zweifel P (2013) The LISA Pathfinder Mission. In: Auger G, Binétruy P, Plagnol E (eds) 9th LISA Symposium, Astronomical Society of the Pacific Conference Series, vol 467, p 5
- Mehta PM, Walker AC, Sutton EK, Godinez HC (2017) New density estimates derived using accelerometers on board the champ and grace satellites. *Space Weather* 15(4):558–576, DOI <https://doi.org/10.1002/2016SW001562>, URL <https://agupubs.onlinelibrary.wiley.com/doi/abs/10.1002/2016SW001562>, <https://agupubs.onlinelibrary.wiley.com/doi/pdf/10.1002/2016SW001562>
- Montenbruck O, Gill E (2000) *Satellite Orbits*, vol 1. Springer-Verlag, Berlin, Heidelberg, DOI 10.1007/978-3-642-58351-3
- NASA (2020a) Mass change designated observable science and applications traceability matrix. URL <https://science.nasa.gov/earth-science/decadal-mc>
- NASA (2020b) The nasa mass change designated observable study agu 2020 town hall. URL <https://science.nasa.gov/earth-science/decadal-mc>
- NASA (2021) General environmental verification standard (gevs) for gsfc flight programs and projects
- National Academies of Sciences Engineering and Medicine (2018) *Thriving on Our Changing Planet: A Decadal Strategy for Earth Observation from Space*. The National Academies Press, Washington, DC, DOI 10.17226/24938, URL <https://www.nap.edu/catalog/24938/thriving-on-our-changing-planet-a-decadal-strategy-for-earth>
- Olatunde T, Shelley R, Chilton A, Serra P, Ciani G, Mueller G, Conklin J (2015) 240 nm uv leds for lisa test mass charge control. *Journal of Physics: Conference Series* 610:012,034, DOI 10.1088/1742-6596/610/1/012034
- Reigber C, Lühr H, Schwintzer P (2002) Champ mission status. *Advances in Space Research* 30(2):129–134, DOI [https://doi.org/10.1016/S0273-1177\(02\)00276-4](https://doi.org/10.1016/S0273-1177(02)00276-4), URL <https://www.sciencedirect.com/science/article/pii/S0273117702002764>
- Sheard B, Heinzel G, Danzmann K, Shaddock D, Klipstein W, Folkner W (2012) Intersatellite laser ranging instrument for the grace follow-on mission. *Journal of Geodesy* 86, DOI 10.1007/s00190-012-0566-3
- Speake CC, Andrews PL (1997) Capacitive sensing for drag - free satellites. *Class Quant Grav* 14:1557–1565,

- DOI 10.1088/0264-9381/14/6/027
- Spero R (2021) Point-mass sensitivity of gravimetric satellites. *Advances in Space Research* 67(5):1656–1664, DOI <https://doi.org/10.1016/j.asr.2020.12.019>, URL <https://www.sciencedirect.com/science/article/pii/S0273117720308759>
- Sumner TJ, Mueller G, Conklin JW, Wass PJ, Hollington D (2020) Charge induced acceleration noise in the LISA gravitational reference sensor. *Classical and Quantum Gravity* 37(4):045,010, DOI 10.1088/1361-6382/ab5f6e, URL <https://doi.org/10.1088/1361-6382/ab5f6e>
- Tapley B, Watkins M, Flechtner F, Reigber C, Bettadpur S, Rodell M, Sasgen I, Famiglietti J, Landerer F, Chambers D, Reager J, Gardner A, Save H, Ivins E, Swenson S, Boening C, Dahle C, Wiese D, Dobsław H, Velicogna I (2019) Contributions of grace to understanding climate change. *Nature Climate Change* 5, DOI 10.1038/s41558-019-0456-2
- Tapley BD, Bettadpur S, Watkins M, Reigber C (2004) The gravity recovery and climate experiment: Mission overview and early results. *Geophysical Research Letters* 31(9), DOI <https://doi.org/10.1029/2004GL019920>, URL <https://agupubs.onlinelibrary.wiley.com/doi/abs/10.1029/2004GL019920>, <https://agupubs.onlinelibrary.wiley.com/doi/pdf/10.1029/2004GL019920>
- Touboul P, Foulon B, Willemenot E (1999) Electrostatic space accelerometers for present and future missions based on paper iaf.96.j1.02 presented at the 47th international astronomical congress, 7–11 october, 1996, beijing, china. *Acta Astronautica* 45(10):605–617, DOI [https://doi.org/10.1016/S0094-5765\(99\)00132-0](https://doi.org/10.1016/S0094-5765(99)00132-0), URL <https://www.sciencedirect.com/science/article/pii/S0094576599001320>
- Touboul P, Rodrigues M, Métris G, Tetry B (2001) Microscope, testing the equivalence principle in space. *Comptes Rendus de l'Académie des Sciences - Series IV - Physics* 2(9):1271–1286, DOI [https://doi.org/10.1016/S1296-2147\(01\)01264-1](https://doi.org/10.1016/S1296-2147(01)01264-1), URL <https://www.sciencedirect.com/science/article/pii/S1296214701012641>
- Weber WJ, Cavalleri A, Dolesi R, Fontana G, Hueller M, Vitale S (2002) Position sensors for LISA drag-free control. *Classical and Quantum Gravity* 19(7):1751–1756, DOI 10.1088/0264-9381/19/7/371, URL <https://doi.org/10.1088/0264-9381/19/7/371>
- Wegener H, Müller V, Heinzl G, Misfeldt M (2020) Tilt-to-length coupling in the grace follow-on laser ranging interferometer. *Journal of Spacecraft and Rockets* 57(6):1362–1372, DOI 10.2514/1.A34790, URL <https://doi.org/10.2514/1.A34790>, <https://doi.org/10.2514/1.A34790>
- Wiese D, Nerem R, Han SC (2011a) Expected improvements in determining continental hydrology, ice mass variations, ocean bottom pressure signals, and earthquakes using two pairs of dedicated satellites for temporal gravity recovery. *Journal of Geophysical Research (Solid Earth)* 116:11,405–, DOI 10.1029/2011JB008375
- Wiese D, Nerem R, Lemoine F (2011b) Design considerations for a dedicated gravity recovery satellite mission consisting of two pairs of satellites. *Journal of Geodesy* 86:81–98
- Wiese DN, Visser P, Nerem RS (2011c) Estimating low resolution gravity fields at short time intervals to reduce temporal aliasing errors. *Advances in Space Research* 48(6):1094–1107, DOI <https://doi.org/10.1016/j.asr.2011.05.027>, URL <https://www.sciencedirect.com/science/article/pii/S0273117711003929>